The MODIS Cloud Optical and Microphysical Products: Collection 6 Updates and Examples From Terra and Aqua

Steven Platnick, Kerry G. Meyer, Michael D. King, Galina Wind, Nandana Amarasinghe, Benjamin Marchant, G. Thomas Arnold, Zhibo Zhang, Paul A. Hubanks, Robert E. Holz, et al.

▶ To cite this version:

Steven Platnick, Kerry G. Meyer, Michael D. King, Galina Wind, Nandana Amarasinghe, et al.. The MODIS Cloud Optical and Microphysical Products: Collection 6 Updates and Examples From Terra and Aqua. IEEE Transactions on Geoscience and Remote Sensing, 2017, IEEE Transactions on Geoscience and Remote Sensing, 55 (1), pp.502-525. 10.1109/tgrs.2016.2610522 . hal-04475244

HAL Id: hal-04475244

https://hal.univ-lille.fr/hal-04475244v1

Submitted on 23 Feb 2024

The MODIS Cloud Optical and Microphysical Products: Collection 6 Updates and Examples From Terra and Aqua

Steven Platnick, Kerry G. Meyer, Michael D. King, *Fellow, IEEE*, Galina Wind, Nandana Amarasinghe,
Benjamin Marchant, G. Thomas Arnold, Zhibo Zhang, Paul A. Hubanks,
Robert E. Holz, Ping Yang, William L. Ridgway, and Jérôme Riedi

Abstract—**The Moderate-Resolution Imaging Spectroradiometer (MODIS) level-2 (L2) cloud product (earth science data set names MOD06 and MYD06 for Terra and Aqua MODIS, respectively) provides pixel-level retrievals of cloud top properties (day and night pressure, temperature, and height) and cloud optical properties (optical thickness, effective particle radius, and water path for both liquid water and ice cloud thermodynamic phases—daytime only). Collection 6 (C6) reprocessing of the product was completed in May 2014 and March 2015 for MODIS Aqua and Terra, respectively. Here we provide an overview of major C6 optical property algorithm changes relative to the previous Collection 5 (C5) product. Notable C6 optical and microphysical algorithm changes include: 1) new ice cloud optical property models and a more extensive cloud radiative transfer code lookup table (LUT) approach; 2) improvement in the skill of the shortwave-derived cloud thermodynamic phase; 3) separate cloud effective radius retrieval data sets for each spectral combination used in previous collections; 4) separate retrievals for partly cloudy pixels and those associated with cloud edges; 5) failure metrics that provide diagnostic information for pixels having observations that fall outside the LUT solution space; and 6) enhanced pixel-level retrieval uncertainty calculations. The C6 algorithm changes can collectively result in significant changes relative to C5, though the magnitude depends on the data set and the pixel's retrieval location in the cloud parameter space. Example L2 granule and level-3 gridded data set differences between the two collections are shown. While the emphasis is on the suite of cloud optical property data sets, other MODIS cloud data sets are discussed when relevant.**

Index Terms—**Aqua, cloud remote sensing, clouds, MOD06, moderate resolution imaging spectroradiometer (MODIS), MYD06, satellite applications, Terra, terrestrial atmosphere.**

I. INTRODUCTION

SINCE the launch of NASA's Terra satellite on December 18, 1999, followed by Aqua on May 4, 2002, the Moderate-Resolution Imaging Spectroradiometer (MODIS) has become one of the most widely used satellite remote sensing platforms for earth science investigations. Designed to provide global observations of the earth's atmosphere, land, and oceans [1]–[4], MODIS measures reflected solar and emitted thermal radiation in 36 spectral channels ranging from the visible (VIS) to the infrared (IR) at a native spatial resolution of 250 m (0.66- and 0.87-μm channels), 500 m [five channels including three shortwave IR (SWIR)], and 1 km (all others). MODIS provides unique spectral and spatial capabilities for retrieving cloud properties. The NASA operational cloud product (earth science data set (SDS) names MOD06 and MYD06 for Terra and Aqua MODIS, respectively, though for simplicity, the modifier MOD will subsequently be used for both Terra and Aqua since the respective algorithms are nearly identical) [5] contains pixel-level retrievals of cloud top properties (pressure, temperature, and height during both day and night) and cloud optical and microphysical properties [cloud optical thickness (COT), effective particle radius (CER), and derived water path (CWP) for both liquid water and ice cloud thermodynamic phases during daytime only] [6].

The cloud top properties' algorithm, which relies on CO_2-slicing channels (13–14-μm spectral region) and two IR window channels [7], [8], has heritage with the high-resolution IR radiation sounder [9]; spatial resolution is at both 5 and 1 km for Collection 6 (C6). The 1-km cloud optical and microphysical product algorithm makes primary use of six VIS, near IR (NIR), SWIR, and midwave IR (MWIR) MODIS channels, as well as several thermal IR channels. Relative to previous generation global imagers such

Manuscript received March 24, 2016; revised August 26, 2016; accepted August 27, 2016. Date of publication October 26, 2016; date of current version November 29, 2016. This work was supported by the Nataionl Aeronautics and Space Administration (NASA) through the MODIS Science Team and the Radiation Sciences Program. The work of M. D. King was supported by NASA to the University of Colorado under Grant NNX14AO70G. The work of R. E. Holz was supported by NASA to the University of Wisconsin under Grant NNX14AO69G.

S. Platnick is with the Earth Sciences Division, NASA Goddard Space Flight Center, Greenbelt, MD 20771 USA (e-mail: steven.platnick@nasa.gov).

K. G. Meyer and B. Marchant are with Goddard Earth Science Technology and Research, Universities Space Research Association, Columbia, MD 21046 USA.

M. D. King is with the Laboratory for Atmospheric and Space Physics, University of Colorado, Boulder, CO 80303 USA, and also with the Texas A&M University Institute for Advanced Study.

G. Wind, N. Amarasinghe, G. T. Arnold, and W. L. Ridgway are with Science Systems and Applications, Inc., Lanham, MD 20706 USA.

Z. Zhang is with the Department of Physics, University of Maryland–Baltimore County, Baltimore, MD 21250 USA.

P. A. Hubanks is with ADNET Systems, Inc., Bethesda, MD 20817 USA.

R. E. Holz is with the Space Science and Engineering Center, University of Wisconsin–Madison, Madison, WI 53706 USA.

P. Yang is with the Department of Atmospheric Sciences, Texas A&M University, College Station, TX 77845 USA.

J. Riedi is with the Laboratoire d'Optique Atmosphérique, Université de Lille–Sciences et Technologies, 59655 Villeneuve d'Ascq, France.

Digital Object Identifier 10.1109/TGRS.2016.2610522

as the Advanced Very High Resolution Radiometer (AVHRR), MODIS has a number of additional spectral channels, including window channels centered near 1.6 and 2.1 μm that, in addition to an AVHRR heritage channel near 3.7 μm, provide cloud microphysical information. The basic physical principle behind the simultaneous retrieval of COT and CER is the bispectral solar reflectance method first described in [10] and applied to airborne data. MOD06-specific heritage work is also described in [11] and [12] (microphysical retrievals using the AVHRR 3.7-μm channel), [13] (1.6–2.1-μm retrievals over snow/ice surfaces), and [14] (thermodynamic phase retrievals).

MODIS (re)processing streams are referred to as data collections. A major increment in the collection number denotes comprehensive changes to the instrument calibration and science algorithms. Collection 5 (C5) was completed in calendar year 2006, while a reprocessing to C5.1 was completed in calendar year 2010. MODIS Atmosphere Team C6 Aqua level-2 (L2), or pixel-level, reprocessing began in December 2013 and was completed in early May 2014 (data acquisition dates July 4, 2002 through December 31, 2013); Aqua forward processing began on January 1, 2014. Atmosphere Team C6 Terra L2 reprocessing began in November 2014 and was completed in March 2015 (data acquisition dates January 24, 2000 through December 31, 2014); Terra forward processing began on January 1, 2015. Atmosphere Team level-3 (L3) (re)processing for Terra and Aqua began in October 2014 and was completed in March 2015.

Basic MOD06 optical property algorithm details are described in the C5 algorithm theoretical basis document (ATBD) addendum [15] and original ATBD [16]. An overview of the MODIS cloud product algorithms (at the time of Collection 4) along with example results is provided in [6] and [17]. C5 algorithm-related work is described in various publications, e.g., ice radiative models [18], [19], multilayer cloud detection [20], [21], clear sky restoral (CSR) filtering [22], [23], pixel-level retrieval uncertainties [24], and global aggregated statistics [25]. Evaluation-specific investigations include cloud phase [26], [27], view angle biases [28]–[30], and the impacts of non-plane-parallel clouds [22], [31], [32].

Due to the significant number of algorithm and data set changes implemented in the latest collection, an overview paper of the C6 MOD06 cloud optical and microphysical property product is warranted. Here we focus on key changes with respect to C5 and the resulting impact to granule-level and global cloud property statistics. The MOD06 cloud optical and microphysical retrieval algorithm is numerically intensive, depending on explicit forward radiative calculations for cloud, gas, and surface interactions. Updates for C6 are representative of evolving passive imager cloud retrieval science as spectral information from MODIS and other capable sensors continues to be explored (e.g., synergistic A-Train [33] studies have provided important constraints on ice particle radiative models [34]). Meanwhile, the climate modeling community continues to improve its ability to exploit the product (see [23]) and cloud assessment reports [35], [36] acknowledge the challenges in establishing cloud climate data records. Note that the MOD06 product should not be confused with a separate MODIS cloud product developed specifically for clouds and the earth's radiant energy system (CERES) processing [37], [38]; comparisons between many CERES Edition-2 and MODIS C5 products are given in [38].

II. SUMMARY OF COLLECTION 6 UPDATES

The C6 MOD06 cloud property product is the culmination of extensive multiyear development and testing. While the theoretical basis of the retrievals remains unchanged from C5, numerous algorithm updates and enhancements have been implemented that increase algorithm sophistication and performance. Note that only updates to the cloud optical and microphysical property retrievals are discussed here; updates to the cloud top property and IR-derived thermodynamic phase algorithms, including the new native 1 km resolution retrievals, are detailed in [8]. Notable updates to the optical and microphysical property retrievals include the following.

1) Radiative transfer and lookup table (LUT) improvements reduce algorithm complexity and maintenance by eliminating the use of asymptotic theory, reduce linear interpolation errors by optimizing LUT grid point locations and separating the single and multiple scattering (MS) components, and include a new single-habit ice cloud radiative model based on the severely roughened aggregate of solid columns [39] that has been shown to provide better retrieval consistency with IR and lidar-based COT retrievals [34].
2) A redesigned cloud thermodynamic phase algorithm, based on a variety of independent tests with assigned weights, provides improved skill in comparison with collocated lidar- and polarimeter-based phase products.
3) Separate spectral retrievals of COT, CER, and derived CWP for channel combinations include the 1.6-, 2.1-, and 3.7-μm channels that allow for independent L3 aggregation and ease retrieval intercomparisons.
4) Separate SDSs for lower quality scenes identified by C5-like CSR algorithms [22] flag pixels not expected to be overcast (referred to as "partly cloudy" (PCL) retrievals), a 1-km subpixel 250-m reflectance heterogeneity index, and an updated multilayer cloud detection scheme [20], [21], [40]; this information can be used for improved retrieval quality assessment.
5) Retrieval failure metrics (RFMs) provide diagnostic information for pixels where the reflectance observations fall outside the LUT solution space.
6) Improved pixel-level retrieval uncertainty estimates include scene-dependent L1B uncertainties [41], cloud model and surface albedo error sources (cloud effective variance, ocean surface wind speed, and direction), and 3.7-μm emission error sources; note that these uncertainties do not include estimates of 3-D radiative transfer biases or ice habit model error sources.
7) Updated handling of surface reflectance, including a new dynamic eight-day sampling surface spectral albedo data set derived from gap-filled C5 Aqua + Terra MODIS data (MCD43B3 [42]), adoption of land spectral emissivities consistent with the cloud top property

algorithm [43], and wind speed interpolated bidirectional reflectance properties of water surfaces based on the parameterization of Cox and Munk [44].

8) A new L1B reaggregation scheme for Aqua MODIS accounts for focal plane misalignment between the 250-m resolution channels (0.66 and 0.87 μm) and the 500-m resolution channels (0.47, 0.55, 1.24, 1.6, and 2.1 μm); note that all maintained atmospheric products for Aqua MODIS use the new reaggregated L1B, including the dark target [45] and enhanced deep blue [46] aerosol products.

A more detailed discussion of the C6 MOD06 cloud optical and microphysical property retrieval algorithm is provided in Section III (note that the above lettering scheme is consistent with the organization of Section III), followed by a discussion of the impacts of the C6 updates on the L3 global gridded cloud property statistics and best practice guidance for MOD06 product users.

III. C6 ALGORITHM DETAILS

A. Cloud Radiative Models

The simultaneous retrieval of COT and CER can be achieved by simultaneously measuring the cloud reflectance in two spectral channels having a different amount of cloud particle absorption (e.g., VIS/NIR and SWIR, respectively) and comparing the measurements with theoretical forward model calculations, as demonstrated with airborne data [10] (see also [11], [12], [47]–[53]). For previous MOD06 collections (C5 and earlier), the theoretical forward model calculations used asymptotic theory ([10], [51], and the references therein) for optically thick atmospheres, coupled with a forward calculated LUT containing spectral cloud reflectance and fluxes at four discrete optically thin COT values. For C6, asymptotic theory has been replaced with cloud reflectance and emissivity LUTs containing the complete range of COT values. This change simplifies code maintenance such that multiple algorithm paths for optically thin and optically thick atmospheres, followed by interpolation between them, are no longer required; in addition, more optically thin COTs are included in the new LUTs. Note that for optically thick atmospheres, the resulting reflectance computations are the same as those obtained from asymptotic theory.

For the C6 LUTs, cloud top reflectance is calculated for six spectral channels, namely, the nonabsorbing 0.66-, 0.86-, and 1.24-μm channels that are primarily sensitive to COT and the absorbing 1.6-, 2.1-, and 3.7-μm channels sensitive to CER. Effective cloud and surface emissivities [12] are also calculated for the 3.7-μm channel, whose TOA radiance has both solar and thermal components due to its location in the MWIR. The plane-parallel discrete-ordinates radiative transfer algorithm [54] is used for the forward RT calculations, ignoring above-cloud atmospheric gaseous absorption in all channels and above-cloud Rayleigh scattering in the 0.66-μm channel; these effects are included on a pixel-level basis during the retrieval process. For calculations over land, a nonreflecting Lambertian surface is assumed. Over oceans, the angular dependence of the ocean surface BRDF is defined as a function of wind speed using the parameterization of [44]. This treatment of ocean surface BRDF is an improvement over C5, which assumed the ocean as a Lambertian surface with a spectrally flat 0.05 albedo (appropriate for diffuse ocean reflectance).

TABLE I
RANGE OF VALUES OF LUT PARAMETERS

Variable	Number of Grid Points	Range
COT	34	[0, 159]
CER (μm)		
liquid water	18	[2, 30]
ice	12	[5, 60]
μ_0	33	[0.15, 1.0]
μ	28	[0.4, 1.0]
$\Delta\varphi$	37	[0°, 180°]
u ($\mathrm{m \cdot s^{-1}}$)	3	[3, 7, 15]

In addition to cloud reflectance (and emissivity as needed), the reflected flux, transmitted flux, and spherical albedo for the above six channels, as well as for the thermal IR channel centered at 11 μm, are also computed and included in the land LUT for use with a pixel-level Lambertian surface albedo data set that is incorporated during the retrieval process. The C6 ocean LUTs also contain effective surface and cloud emissivities for the 3.7- and 11-μm channels, the latter needed for modifying low cloud MOD06 cloud top temperature (CTT) retrievals by accounting for nonunity cloud emissivity. While the cloud top property algorithm [8] retrieves low cloud properties assuming unity emissivity in the IR window, the optical property algorithm iterates on that solution using cloud emissivities calculated from the COT retrieval and without regard to potential nonunity cloud fraction within the pixel (see CSR discussion in Section III-D). Effective emissivity calculations in both spectral channels follow the approach described in [12]. For the land LUTs, effective emissivities are calculated from forward-modeled flux and spherical albedo data. The LUT parameters are stored as a function of a defined range of COT, CER, and observation angle geometry [i.e., cosines of the solar (μ_0) and sensor (μ) zenith angles, and relative azimuth ($\Delta\varphi$)], as well as surface wind speed for the ocean LUTs. Note that the ocean LUTs do not explicitly account for wind direction; LUT values are averages of RT calculations at the four principal wind directions, i.e., 0°, 90°, 180°, and 270° relative azimuth. Details of these defined ranges are provided in Table I. A minimum ice CER of 5 μm has continued to be used for consistency with C5 [18] because retrievals below this value are relatively infrequent.

To minimize angular interpolation errors, only the MS component of the cloud top reflectance (R) is calculated and stored in the LUTs; the single scattering (SS) component is calculated during the retrieval process from the exact phase function (PF) using pixel-level geometric information,

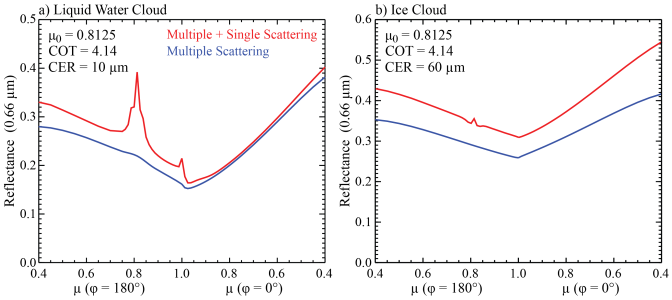

Fig. 1. Total (red line) and MS (blue line) cloud top reflectance for MODIS channel 1 (0.66 μm) for (a) liquid water clouds with CER = 10 μm and (b) ice clouds (severely roughened aggregated columns) with CER = 60 μm. All calculations assume COT = 4.14 and $\mu_0 = 0.8125$. The MS component is much smoother than the total reflectance that includes single plus MS.

and is added dynamically to the interpolated MS component. For example, at a particular sun–satellite geometry, the SS part of the bidirectional reflectance (R_{ss}) is calculated from the PF, such that

$$R_{\mathrm{ss}}(\tau, r_e, \mu, \mu_0, \Delta\varphi) = \frac{1}{4(\mu+\mu_0)}\frac{\omega_0}{1-f\omega_0}\mathrm{PF}(\Theta, r_e)\left(1-\exp\left[\tau'\left(\frac{1}{\mu}+\frac{1}{\mu_0}\right)\right]\right) \tag{1}$$

where $\tau' = (1 - f\omega_0)\tau$, r_e denotes CER, Θ is the scattering angle, f is the PF truncation factor (i.e., the fraction of photons in the PF forward peak due to diffraction), and ω_0 is the SS albedo. The total cloud top reflectance is then found by adding R_{SS} to the MS reflectance component that is interpolated from the LUTs. MS and total reflectance (MS + SS) at 0.66 μm as a function of sensor zenith angle in the forward and backscattered directions are shown in Fig. 1 for an example (a) liquid and (b) ice phase cloud. It is evident that the MS part of the reflectance (blue lines) is a smoother function compared with the total (MS + SS) reflectance (red lines), thus the angular features of the total reflectance arise from the SS component, and calculating the exact SS component minimizes LUT interpolation errors.

In addition to separating the MS and SS reflectance components, the COT, μ, and μ_0 LUT grid point spacing are also optimized to further minimize interpolation errors. For μ and μ_0, LUT grid point spacing for C6 is 0.05 at μ and μ_0 values less than 0.75, and 0.0125 for values between 0.75 and 1.0. Analysis of this discretization scheme has shown that typical full reflectance LUT interpolation errors averaged over all COT, CER, and relative azimuth are on the order of 0.1%–0.2% reflectance. Furthermore, compared with other μ and μ_0 discretization schemes considered during C6 development, this scheme also yields the smallest maximum interpolation error for the MS reflectance component, in particular at nadir ($\mu = 1$), as shown by the polar plots in Fig. 2. Here, the maximum interpolation error at $\mu_0 = 0.725$ for (a) an ice cloud with COT = 4.14 and CER = 30 μm and (b) a liquid water cloud with COT = 4.14 and CER = 10 μm is shown for three μ discretization schemes, namely, the scheme selected for C6 (right column) as well as schemes with grid spacing of 0.05 (left column) and 0.025 (center column) across all μ. Note the sensor zenith μ varies from 1.0 at the center of each plot to 0.4 at plot edge, and the relative azimuth varies clockwise around each plot from 0° to 360°.

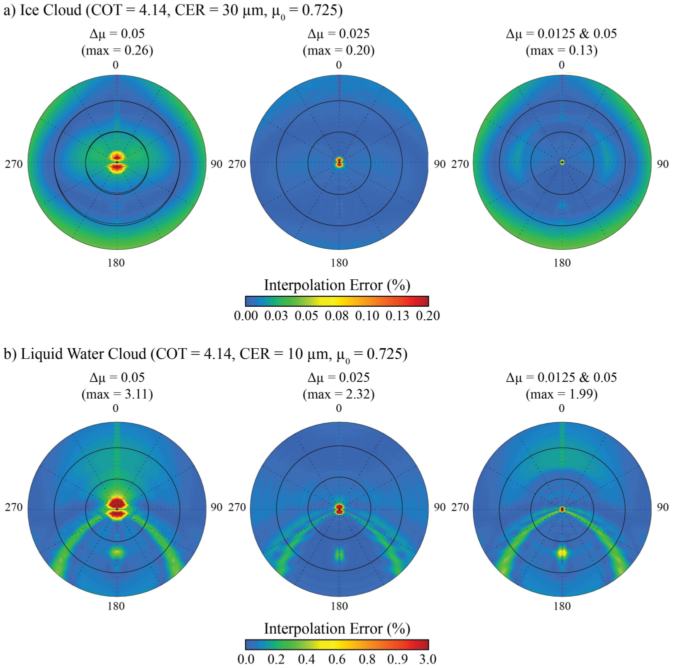

Fig. 2. Maximum MS reflectance interpolation error for COT = 4.14 and $\mu_0 = 0.725$ for (a) ice clouds with CER = 30 μm (severely roughened aggregated columns) and (b) liquid water clouds with CER = 10 μm. The hybrid LUT discretization scheme adopted for C6 (right column) has the least error near nadir.

To create the LUTs, the forward RT calculations of cloud top reflectance require appropriate radiative transfer models that include the SS properties of liquid and ice phase clouds. For liquid phase clouds, the C6 SS properties are identical to those of C5, and are computed from Mie calculations assuming a modified gamma droplet size distribution with an effective variance of 0.1. Wavelength-dependent liquid water complex refractive indices are obtained from [55] for visible wavelengths through 1.0 μm, [56] for $1.0 < \lambda < 2.6$ μm, and [57] for $\lambda > 3.5$ μm.

For ice phase clouds, however, significant changes to the radiative transfer model are introduced for C6. Comparisons of forward RT calculations with satellite remote sensing using polarization of reflected sunlight from polarization and directionality of the earth's reflectances (POLDER) suggest that ice crystals with roughened surfaces significantly outperform smooth ice crystals [58]. Moreover, reflectance-based COT retrievals using a single habit, namely, severely roughened compact aggregates composed of eight solid columns (hereafter referred to as aggregated columns) [39], were found to provide closure with thermal IR-based retrievals and are in better agreement with cloud-aerosol lidar with orthogonal polarization (CALIOP) [34]. Based on the aforementioned sensitivity studies, the smooth ice crystal size/habit distribution cloud models used in C5 [18] have been replaced with a gamma particle size distribution (effective variance 0.1) consisting of these severely roughened aggregated columns.

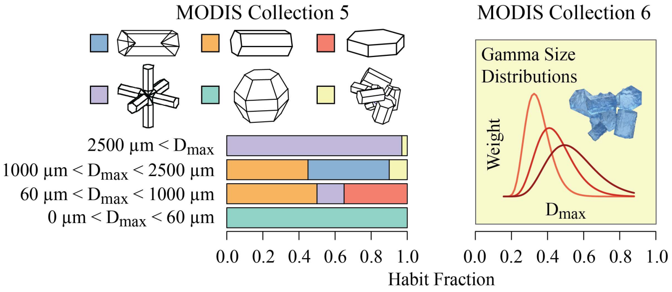

Fig. 3. (Left) MODIS C5 ice model with habit mixture prescribed as a function of particle size. (Right) MODIS C6 single habit ice model along with example analytic gamma size distributions used for C6 radiative calculations.

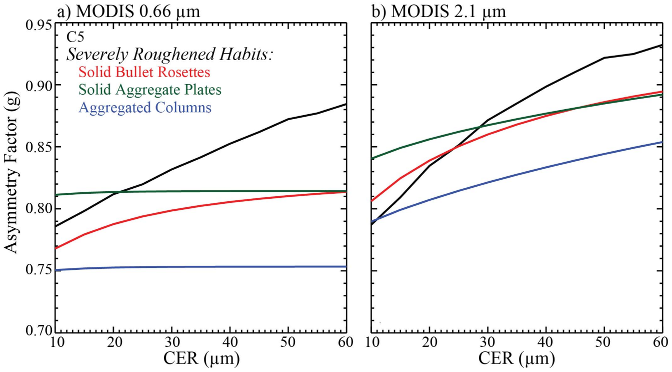

Fig. 4. Asymmetry factor as a function of CER for ice crystals having the size/habit distribution used in C5 (black line), and gamma distribution of severely roughened solid bullet rosettes (red line), solid aggregate plates (green line), and the aggregated columns used in C6 (blue line) for the (a) 0.66- and (b) 2.1-μm wavelength channels. Note that ice crystals having severely roughened surfaces have significantly smaller asymmetry factors than those assumed in C5.

Fig. 3 schematically illustrates the C5 (left) and C6 (right) ice crystal habit models. With respect to ice crystal habit mixture, the C5 model assumed four broad size bins defined in terms of the particle maximum dimension ($D_{\max}$): 100% droxtals for $0 < D_{\max} < 60$ μm; 15% bullet rosettes, 60% solid columns, and 35% plates for $60 \mu\text{m} < D_{\max} < 1000$ μm; 45% hollow columns, 45% solid columns, and 10% aggregates for 1000 $\mu\text{m} < D_{\max} < 2500$ μm; and 97% bullet rosettes and 3% aggregates for 2500 $\mu\text{m} < D_{\max}$.

Fig. 4 shows the effect of using severely roughened ice crystals on calculations of the asymmetry factor, g, at the (a) 0.66- and (b) 2.1-μm wavelength channels. For the habits considered here (solid bullet rosettes, solid aggregate plates, and aggregated columns), roughened particles generally yield smaller asymmetry factors than the C5 models (black lines). To ascertain how decreasing the asymmetry parameter affects retrievals of COT, recall that the quantity $\tau(1 - \omega_o g)$, where τ refers to COT, has been found to be invariant [59]; for a nonabsorptive channel (i.e., $\omega_o \rightarrow 1$), this reduces to $\tau(1-g)$, a quantity known as the "effective optical thickness" [59]. It then follows that differences between C5 COT retrievals and those using roughened particles (C6) can be approximated by

$$\frac{\tau^{C6}}{\tau^{C5}} \approx \frac{1 - g^{C5}(r_e)}{1 - g^{C6}(r_e)}. \tag{2}$$

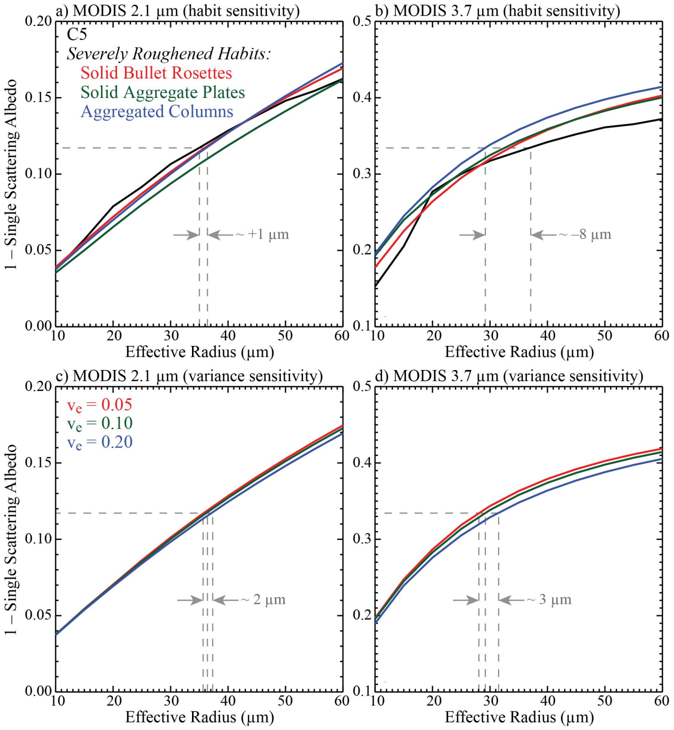

Fig. 5. Simulations of coalbedo as a function of CER for crystals having the size/habit distribution used in C5 (black line), and gamma distribution of severely roughened solid bullet rosettes (red line), solid aggregate plates (green line), and the aggregated columns used in C6 (blue line) for the (a) 2.1- and (b) 3.7-μm wavelength channels. Ice crystals having severely roughened surfaces have smaller (larger) absorption than those assumed in C5 at 2.1 μm (3.7 μm), which can potentially lead to larger (smaller) values of CER in C6. Calculations of coalbedo for severely roughened aggregated columns at various values of effective variance are given for (c) 2.1 and (d) 3.7 μm.

Thus, using roughened ice crystals will yield smaller COT retrievals than those of C5, which have been shown to be biased high in the case of COT retrievals of optically thin clouds, i.e., those that can be retrieved by MODIS IR techniques and CALIOP [34]. Similarly, comparisons of MODIS Aqua COT retrievals against the AIRS IR spectrometer version 6 product show excellent agreement for single-layer low-latitude ice clouds [60].

In addition to cloud asymmetry factor differences, the cloud SS albedo (ω_0) derived from the new roughened ice crystal models is also generally larger at the absorbing SWIR wavelengths, as shown in Fig. 5 by the smaller values of coalbedo 1-ω_0 for the 2.1-μm MODIS channel (a). For the MWIR 3.7-μm channel (b), 1-ω_0 is larger than that found in C5. Because the SWIR and MWIR wavelength channels are primarily used to infer particle size, assuming that roughened ice crystals will often lead to larger values of CER at 2.1 μm than the smooth ice crystal models of C5 and smaller values of CER at 3.7 μm, due to changes in ω_0 alone; note that CER retrieved from the 2.1-μm channel will be larger still due to the reduction in asymmetry factor g shown in Fig. 4, since forward calculated cloud top reflectance will increase with decreasing g at constant CER. The sensitivity of ω_0 at 2.1 and 3.7 μm to the effective variance (v_e) of the assumed gamma size distribution of roughened aggregate columns is shown in Fig. 5(c) and (d), respectively. Although the true

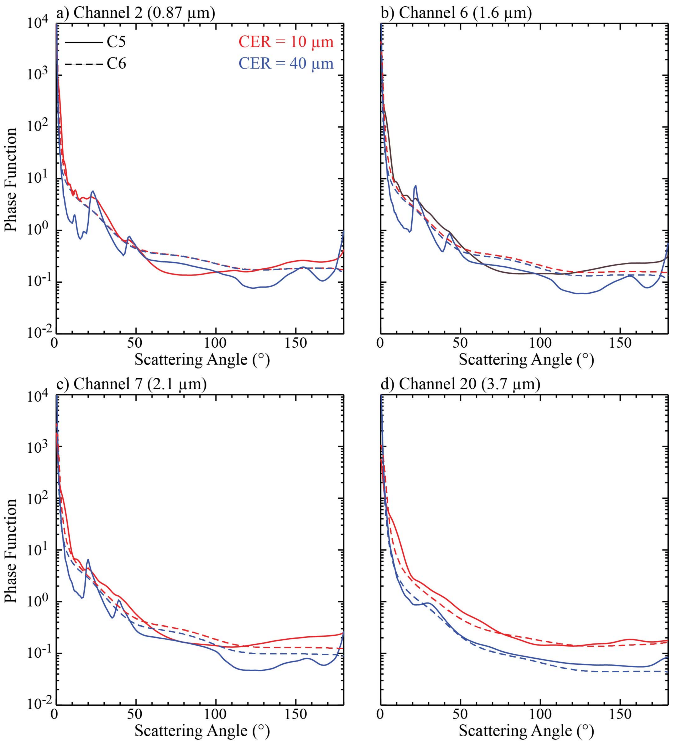

Fig. 6. C5 (solid line) and C6 (dashed line) ice model PFs at four wavelength channels for CER = 10 μm (red line) and 40 μm (blue line).

effective variance of ice clouds is not known, a value of 0.1 was chosen for the C6 models, consistent with the liquid water gamma distribution models; the sensitivity to this assumption is considered in calculating retrieval uncertainty estimates (see Section III-F).

An example of the C6 ice model PFs (dashed lines) for four MODIS channels (0.87, 1.6, 2.1, and 3.7 μm) is shown in Fig. 6 along with the corresponding C5 PFs (solid lines). PFs for CER = 10 and 40 μm are shown as red and blue lines, respectively. Note that introducing surface roughness yields smoother PFs for each channel.

As a convenience for the user, C6 MOD06 files now provide SDSs of extinction efficiency, asymmetry factor, and SS albedo for both the ice and liquid water cloud radiative models as a function of spectral channel and CER. This allows a user to estimate appropriate adjustments [e.g., (2)] for comparisons with retrieval methods or radiative models that use different particle scattering assumptions.

B. Cloud Thermodynamic Phase

Because ice and liquid phase clouds have very different scattering and absorbing properties, an incorrect cloud phase decision can lead to substantial errors in COT, CER, and CWP. MOD06 provides two independent cloud phase products, namely, an IR product that infers cloud phase using three channel pairs, i.e., 7.3/11, 8.5/11, and 11/12 μm [8], and a product that uses a combination of SWIR and IR tests [61] whose results are used to determine the processing path for the cloud optical and microphysical property retrievals (hereafter referred to as the COP phase algorithm). The COP phase algorithm categorizes a cloudy pixel as liquid, ice, or undetermined phase. While the undetermined phase category is assigned when the phase tests produce ambiguous results, pixels in this category are nonetheless processed as liquid phase. However, their resulting retrieval statistics are aggregated into separate SDSs in the L3 product (i.e., with the_*Undetermined* suffix). In addition, the COP phase algorithm provides phase results for all cloudy pixels regardless of the success of the cloud optical and microphysical retrievals.

For C6, the COP phase algorithm has been completely redesigned. Changes include a new voting logic versus the sequential decision tree logic of C5 that included individual spectral MOD35 cloud mask tests [14], as well as replacement of the C5 SWIR/NIR reflectance ratio tests with logic utilizing separate ice and liquid phase spectral CER retrievals (though the ratio tests are retained for optically thin clouds over snow and ice surfaces). The voting weights of the new COP phase algorithm have been optimized via extensive global and regional comparisons between Aqua MODIS and CALIOP, and have yielded improved phase determination skill over C5, particularly for broken clouds as well as optically thin ice cloud edges previously misidentified as liquid cloud phase; a similar improvement is observed with respect to collocated polarimetric observations from POLDER.

Four main categories of tests comprise the C6 COP phase algorithm.

1) *IR Phase Test:* This test uses the 1-km IR phase product of Baum *et al.* [8] that is part of the MOD06 cloud top property algorithm.
2) *CTT Tests:* These tests use the MOD06 1-km CTT retrievals. Note that the C5 warm cloud sanity check, in which the phase is forced to liquid when CTT $>$ 270 K, was retained in modified form for C6 (mainly as a larger liquid phase vote) only when the retrieved liquid phase COT $>$ 2.
3) *1.38 μm Test:* This test uses the 1.38-μm high cloud flag from the MOD35 cloud mask product. The capacity of this test to discriminate high-altitude ice clouds from low-altitude liquid clouds is based on the strong water vapor absorption at 1.38 μm [62]. This test is applied only when sufficient water vapor is present, roughly 1 cm precipitable water, and when ice phase COT $<$ 2 to avoid spurious ice votes in the case of optically thick low altitude liquid clouds. In C5, this test was used only when the IR cloud phase decision was undetermined.
4) *Spectral CER Tests*: These tests replace the C5 SWIR/NIR reflectance ratio tests. It is difficult to define linear reflectance ratio thresholds to discriminate ice and liquid phase pixels since reflectance ratios can depend on COT, viewing geometry, and so on; CER retrievals implicitly account for such dependencies. Fig. 7 shows an example of the 0.86–2.1-μm COT and CER retrieval solution space for liquid (red curves) and ice (blue curves) phase clouds over a dark surface for the geometry specified in the caption. Some of the solution space is unambiguously liquid and some unambiguously ice, but there are overlapping regions in which either phase can yield a viable physical solution. Comparison of liquid and ice phase CER retrievals from all

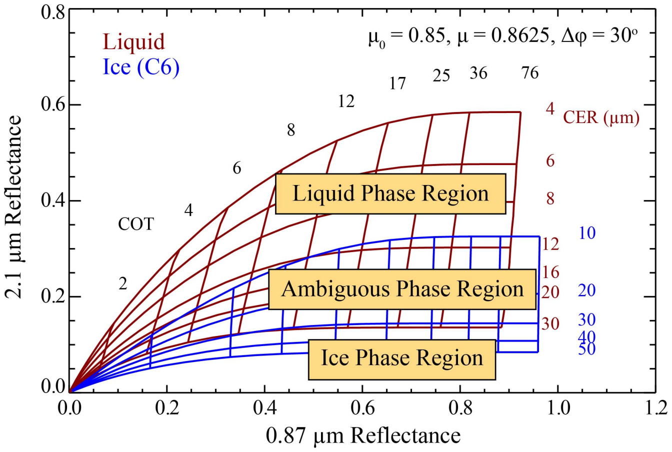

Fig. 7. Theoretical relationship between top-of-cloud reflectance in the 0.87- and 2.1-μm MODIS channels for liquid water (red line) and the C6 ice cloud model (blue line) for various values of COT and CER. Reflectance observations can occur in regions of the solution space that are unambiguously liquid or ice, but may also lie in regions that are ambiguous regarding phase.

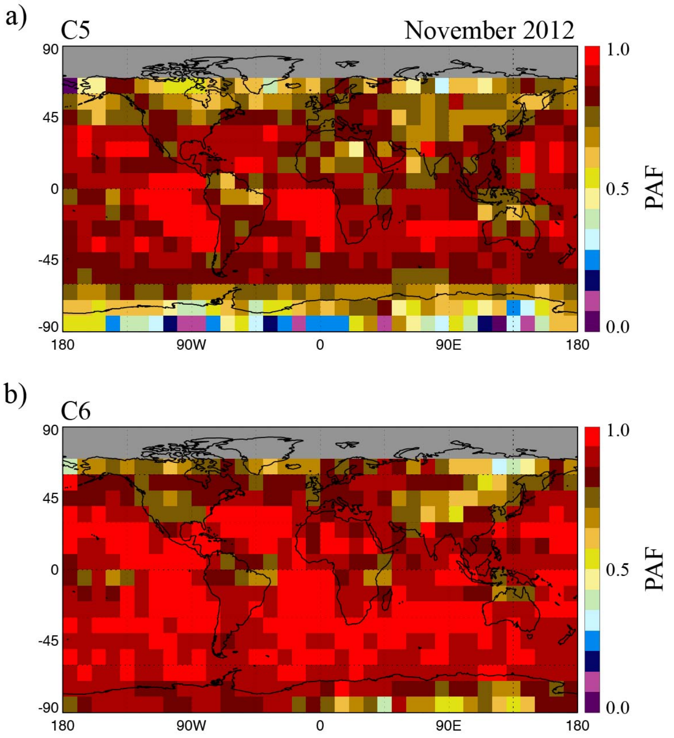

Fig. 8. Global gridded PAF for the (a) C5 and (b) C6 COP thermodynamic phase algorithms for November 2012.

three SWIR/MWIR wavelengths can reduce ambiguity in the choice of thermodynamic phase. Thus, the C6 COP phase algorithm requires six independent pixel-level retrievals, specifically liquid and ice phase CER at 1.6, 2.1, and 3.7 μm.

To evaluate the performance of the new C6 COP phase algorithm, extensive comparisons were performed with the collocated CALIOP cloud layer products. To quantify algorithm skill, we define a phase agreement fraction (PAF) as the number of MODIS pixels where the C6 and CALIOP phase are in agreement divided by the total number of collocated cloudy pixels. Fig. 8 shows the global November 2012 PAF score on a 10° × 10° grid for (a) C5 and (b) C6 for the pixel population identified as "overcast" by the CSR algorithm (CSR $=0$ designation, see Section III-D for details). The C6 cloud phase improvement is broadly distributed, with a notable improvement over ocean. Moreover, the C5 cloud phase skill gradually decreased with increasing latitude, having a pronounced minimum over Antarctica, a shortcoming that has been greatly reduced for C6. Additional comparison results, as well as algorithm details, can be found in [61]. Comparisons of MODIS Aqua phase retrievals against the AIRS IR spectrometer version 6 algorithm are discussed in [60].

C. Separate Spectral Cloud Retrievals

To complement the heritage retrievals using the 2.1-μm channel, COT, CER, and CWP retrievals are now performed and reported separately for channel pairs that include the 1.6- and 3.7-μm channels. These spectral retrievals were also performed in C5, though they were reported only as differences with respect to 2.1 μm [i.e., CER(1.6 μm)–CER(2.1 μm) and CER(3.7 μm)–CER(2.1 μm)], with the 'primary' suite of absolute retrievals being reported only for 2.1 μm. Note that C6 continues to provide a separate retrieval using the 1.6- and 2.1-μm channel pair over snow/ice and ocean surfaces [13]. By reporting the retrievals separately for all channel pairs, it is now possible to do analysis and L3 aggregations that ease spectral retrieval intercomparisons. Table II shows the new C6 SDSs and the difference from C5.

In addition to the desired result of enabling easy intercomparisons among the different retrieval outcomes, it is important to appreciate that the primary three spectral cloud retrievals can have dramatically different failure patterns [63]. For example, retrievals may fail (i.e., the observed reflectance pair lies outside the LUT solution space) when using a visible or NIR (VNSWIR) and SWIR 2.1-μm channel pair, but may yield a successful retrieval when using a VNSWIR and 3.7-μm channel pair. Therefore, the pixel population comprising one retrieval pair may be significantly different than another; this can be particularly true for broken liquid water cloud scenes where cloud heterogeneity scales are on the order of, or less than, the 1-km nadir pixel resolution and/or for cases where a significant drizzle mode is found in the column [64], [32]. Thus, the C5 sampling of spectral CER differences, for instance, between 3.7 and 2.1 μm, was dependent not only on the 3.7-μm retrieval success rate, but on the 2.1-μm retrieval success rate as well. The C5 removal of successful spectral CER retrievals due to filtering by successful 2.1-μm retrievals also leads to a systematic shift in the CER retrieval histogram, as illustrated by the histograms in Fig. 9 derived from a Terra MODIS granule obtained on April 1, 2005 (0635UTC). Here liquid (red lines) and ice (blue lines) phase 3.7-μm CER retrieval histograms are shown for C5 (dashed lines) and C6 (solid lines). The effect on liquid water retrievals is greater because liquid water 2.1-μm CER retrievals tend to fail more often than those at 3.7 μm. Global spectral CER statistics are shown in Section IV.

TABLE II
MAIN CLOUD OPTICAL PROPERTY SDS LISTING

Spectral Retrieval	C5 SDS Name	C6 SDS Name
Optical Thickness 1.6µm	N/A	Cloud_Optical_Thickness_16
Effective Radius 1.6µm	Effective_Radius_Difference (plane 1)	Cloud_Effective_Radius_16
Water Path 1.6µm	N/A	Cloud_Water_Path_16
Optical Thickness 2.1µm	Cloud_Optical_Thickness	Cloud_Optical_Thickness
Effective Radius 2.1µm	Cloud_Effective_Radius	Cloud_Effective_Radius
Water Path 2.1µm	Cloud_Water_Path	Cloud_Water_Path
Optical Thickness 3.7µm	N/A	Cloud_Optical_Thickness_37
Effective Radius 3.7µm	Effective_Radius_Difference (plane 2)	Cloud_Effective_Radius_37
Water Path 3.7µm	N/A	Cloud_Water_Path_37
Optical Thickness 1.6-2.1µm	Cloud_Optical_Thickness_1621	Cloud_Optical_Thickness_1621
Effective Radius 1.6-2.1µm	Cloud_Effective_Radius_1621	Cloud_Effective_Radius_1621
Water Path 1.6-2.1µm	Cloud_Water_Path_1621	Cloud_Water_Path_1621

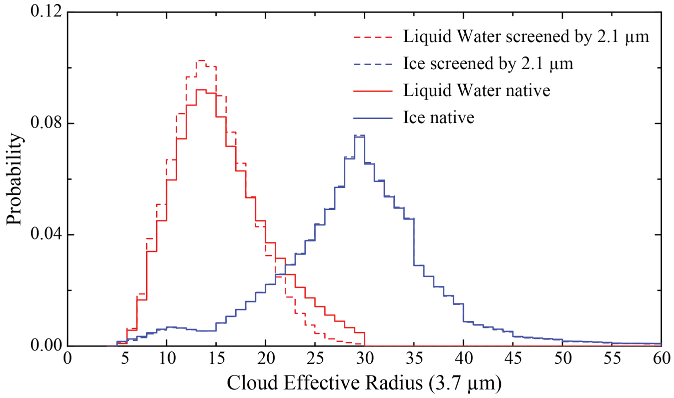

Fig. 9. C6 3.7-μm CER retrieval histograms derived from a Terra MODIS granule obtained on April 1, 2005 (0635UTC). Here liquid phase (red lines) and ice phase (blue lines) histograms are shown for C5 (dashed lines) and C6 (solid lines). The C5 removal of successful spectral CER retrievals due to filtering by successful 2.1-μm retrievals leads to a systematic shift in the CER retrieval histogram.

D. Quality Assurance Considerations: Processing of Partly Cloudy Pixels and Multilayer Cloud Detection

Identifying cloudy pixels appropriate for the MOD06 cloud optical and microphysical property retrievals is largely accomplished using the results from the MOD35 1-km cloud mask tests (note that there are also two 250-m cloud mask spectral tests that can independently report the 1-km cloudy designations as clear sky with a separate set of bits). However, because MOD35 is designed to identify "not clear" pixels, certain situations exist in which pixels identified by MOD35 as "cloudy" are nevertheless likely to be poor retrieval candidates. For instance, near the edge of clouds or within broken cloud fields, a given 1-km MODIS field of view (FOV) may in fact only be partially cloudy. This can be problematic for the MOD06 retrievals because in these cases, the assumptions of a completely overcast homogenous cloudy FOV and 1-D plane-parallel radiative transfer no longer hold, and subsequent retrievals will be of low confidence. Furthermore, some pixels may be identified by MOD35 as "not clear" for reasons other than the presence of clouds, such as scenes with thick smoke or lofted dust, and should therefore not be treated as clouds. With such situations in mind, a CSR algorithm was introduced in C5 that attempts to identify pixels expected to be poor retrieval candidates.

All MOD35 "cloudy" pixels pass through the CSR logic and are assigned four possible outcomes.

1) *Overcast Cloudy (CSR = 0):* Pixels that are not identified as clear or PCL by the CSR tests. Note that MOD35 "not cloudy" pixels will also have CSR = 0.
2) *Not Cloudy (CSR = 2):* Pixels identified by cloud altitude (1-km MOD06 cloud top product coupled with 1.38-μm reflectance), VIS or NIR spatial reflectance variability, and VIS through SWIR spectral curvature tests as likely dust, smoke, or sunglint pixels, and are restored to clear sky.
3) *PCL (CSR = 3):* Pixels over water surfaces that are identified by subpixel 250-m MOD35 cloud mask variability as PCL.
4) *Cloud Edge (CSR = 1):* Overcast cloudy pixels (CSR = 0) with "clear" adjacent neighbors (i.e., adjacent pixels with MOD35 "not cloudy" or CSR = 2).

C6 updates to the CSR algorithm primarily focused on improving the skill of the CSR = 2 category. For instance, the

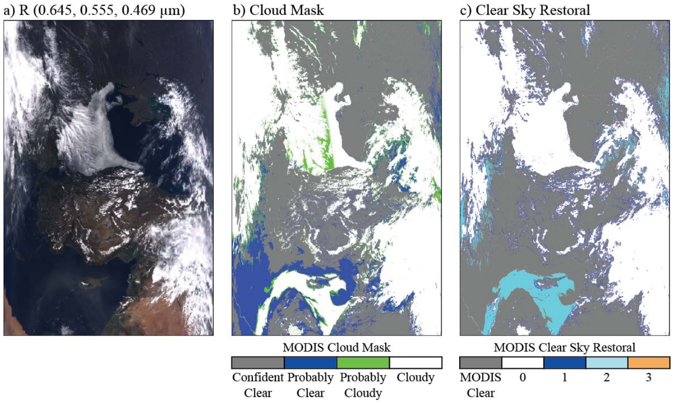

Fig. 10. (a) True color RGB (0.66–0.55–0.47 μm) from an Aqua MODIS granule on April 9, 2005 (1050UTC). (b) MOD35 cloud mask results. (c) MOD06 C6 CSR algorithm results (0: overcast; 1: cloud edge; 2: restored to clear sky; and 3: PCL).

spatial variability tests employed in C5 were not without issue. It was possible to obtain an aerosol-like spatial variability signature from very uniform optically thin marine stratus clouds. As a result, the CSR algorithm often created "holes" in cloud regions where retrievals should have been attempted. To remedy this issue, a neural net-based fast aerosol optical depth (AOD) retrieval algorithm was implemented with code from the Goddard Modeling and Assimilation Office used in GEOS-5 aerosol data assimilation. The algorithm was designed to operate in cloud-free conditions (used internally by GEOS-5 and not described in the literature). When this algorithm is applied to all MODIS pixels placed into the CSR = 2 category, two distinct pixel populations emerge. One population has a reasonable AOD retrieval, while the other gives large values outside of the expected range. For present purposes, optical depth values with $\log(\text{AOD} + 0.01) > 0.95$ are assumed to be associated with cloudy scenes and the CSR category is reset to cloudy.

Fig. 10 shows the CSR results for an example granule from Aqua MODIS, observed on April 9, 2005 (1050UTC) over the Black Sea, Turkey, and the eastern Mediterranean Sea. What appears to be lofted dust is apparent over the Mediterranean at the bottom of the true color RGB (0.66–0.55–0.47 μm) in (a), and is identified as "cloudy," or not clear, by the MOD35 cloud mask (b). This feature is correctly identified by the CSR algorithm (c), and is restored to clear sky by the CSR = 2 tests (light blue shade). Also note the CSR = 1 cloud edge pixels, visible as the regions of dark blue outlining the cloud features in the CSR image.

An important change for C6 is the handling of the so-called "PCL" pixel population that includes both the PCL CSR = 3 and cloud edge CSR = 1 pixels. Previously in C5, MOD06 cloud optical and microphysical retrievals were attempted only on cloudy pixels designated as overcast (CSR = 0) by the CSR algorithm. This implicit retrieval quality filtering necessarily limited the MOD06 retrieval population to those pixels thought to be appropriate for the homogeneous 1-D plane-parallel assumption, and was driven by a desire to provide retrievals of the highest quality. Nevertheless, this denied users the ability to use retrievals of the PCL pixels in an informed manner if they so chose and likely biased retrieval statistics toward optically thicker clouds. For C6, optical and microphysical retrievals are now attempted on these PCL pixels, though in order to reduce their unintentional use, such successful retrievals are reported independently from overcast pixels in SDSs with a *_PCL* suffix identifier in the name.

Retrieval quality is also informed by the multilayer cloud detection algorithm [20], [21]. In C5, the multilayer cloud detection results were stored as an SDS with a confidence flag ranging from one (single-layer cloud) to eight (highest confidence multilayer cloud) based on which multilayer tests were positive; the results were also placed into the *Quality_Assurance_1 km* SDS and combined with thermodynamic phase results to provide, e.g., "single layer ice cloud," and "multilayer ice cloud" information. In C6, the algorithm is updated so that the SDS now contains a total skill score. The skill score is a sum of individual test contributions with each test having a value based on its quality of detection result. Furthermore, two additional tests were added in C6. One test is based on the difference in COT between the VNSWIR and the 1.6–2.1-μm retrievals when the phase is indicated as ice. Large COT retrieval differences (e.g., COT < 30 for the VNSWIR and COT > 80 for the 1.6–2.1-μm retrieval) can indicate the presence of multilayer cloud. The second test included in C6 is the Pavolonis–Heidinger (PH) multilayer cloud retrieval [40]. It was found, however, that when executed globally, the PH algorithm often identifies moderately thick single layer ice clouds as being multilayered; this result was consistent with expectations from a synthetic multilayer radiance study [20]. The scale of overdetection was such that it was decided late in C6 development not to include pixels only identified by the PH algorithm in the L3 multilayer statistical aggregations, even though the result of the PH algorithm is still included in the total skill score. In order to identify which tests contributed to the total skill score, a sixth byte was included in the 1-km QA SDS to indicate the specific test(s) that were triggered. Users are strongly advised to use that QA information in conjunction with the SDS skill score and exclude areas where only the PH test is positive. The PH algorithm may be removed from consideration if further reprocessing is deemed to be warranted by the science team.

In summary, to identify potentially multilayer cloud pixels in MOD06, it is recommended that users look carefully at the 1-km QA Byte 6 and use the same filtering methodology used by the MOD06 team for L3 multilayer statistical aggregations as described above. Because of the high weighting given to the PH test in early C6 development, users should not use the *Cloud_Multi_Layer_Flag* SDS to infer overall confidence in the multilayer detection result.

E. Retrieval Failure Metric

Even if an optical/microphysical retrieval attempt fails, i.e., the observed pixel reflectance pair lies outside the LUT solution space such that the standard solution logic fails to produce a successful COT/CER retrieval pair, the location of the pixel's observed reflectance with respect to the LUT can provide information useful in understanding the radiative equivalent COT and CER; note that a less frequent failure type

TABLE III
MAPPING OF RETRIEVED SOLUTIONS AND CM FROM THE SOLUTION SPACE REGIONS IN FIG. 11 TO THE RFM SDS

Region	Band Pairs	Retrieval Failure Metric SDS		
		COT	CER	Cost Metric (CM)
Solution Space Interior				
Successful Solution	All	Fill	Fill	Fill
Multiple CER Solution	All	Valid	Valid	≥0
Solution Space Exterior				
IV, VI	All	Fill	Fill	Max
I	All	Fill	Fill	Fill
II, III	All	Nearest LUT COT	Nearest LUT CER	≥0
V	1.6-2.1µm	Fill	Valid	≥0
	All Others	Fill	Fill	Fill

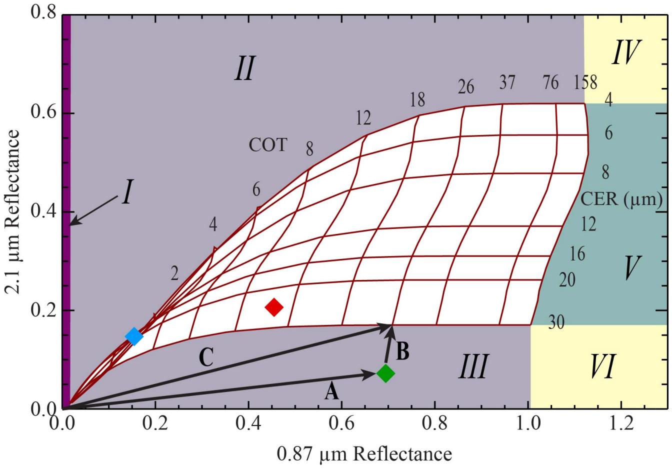

Fig. 11. Retrieval space for a liquid phase cloud over an ocean surface ($\theta_0 = 19.89°$, $\theta = 22.39°$, $\Phi = 174.4°$, and wind speed $= 7\ \mathrm{m \cdot s^{-1}}$), highlighting RFM categories and CM assignments (see Table III). Also shown are example pixels illustrating a successful retrieval (red marker), a retrieval outside the solution space (green marker), and a multiple CER solution retrieval (blue marker). The vectors **A**, **B**, and **C** are used for computing the CM (3) for the pixel outside the solution space. The same logic also applies to ice cloud retrievals (see the example solution space in Fig. 7).

involves observations that lie within the solution space but yield multiple CER solutions. Previously in C5, pixels outside the solution space resulted in either partial COT retrievals (i.e., COT retrieved assuming a CER of 10 or 30 μm for liquid or ice phase clouds, respectively) with CER assigned fill values, or completely failed retrievals with both COT and CER assigned fill values; pixels inside the solution space with multiple possible CER solutions were assigned the largest valid CER solution. For C6, an alternate solution logic (ASL) algorithm is now implemented that gives the COT and/or CER of the LUT grid point closest to the observation, as well as a cost metric (CM) indicating the relative distance of the observation from the LUT solution space.

The ASL is schematically illustrated by the 0.87- and 2.1-μm channel liquid water phase LUT in Fig. 11, where the observation, denoted by the green diamond, is located below the edge of the solution space. The vector **B** points from the observation to the closest LUT point, which, for this pixel, would yield a retrieved COT of 26 and a 30-μm CER. The closest LUT point is selected using a CM, defined here as

$$CM = 100 \left| \frac{\mathbf{B}}{\mathbf{A}} \right| = 100 \left| \frac{\mathbf{C} - \mathbf{A}}{\mathbf{A}} \right| \tag{3}$$

where the vectors **A** and **C** are distances from the origin to the observation point and LUT grid point, respectively. Thus, the CM is essentially a measure of the percent relative distance between the observation and the closest LUT COT and CER grid point.

The COT and/or CER and CM of failed retrievals for all channel pairs, reported in the *Retrieval_Failure_Metric* (RFM) SDSs, can be used to help diagnose retrieval failure causes and provide failure statistics as discussed in [63] for liquid water marine clouds. In order to make RFM assignments, the exterior of the LUT solution space is divided into six regions as shown by the shaded areas surrounding the example liquid water phase LUT in Fig. 11. Also shown are example pixel locations illustrating a successful full retrieval in the LUT interior (red diamond), a retrieval within the LUT interior having multiple CER solutions (ASL solution, blue diamond), and a retrieval in the LUT exterior (ASL solution, green diamond).

Table III provides an overview of the RFM SDS assignments for each region of the solution space in Fig. 11; regions outside of the LUT are labeled *I* through *VI*. These SDSs will be assigned fill values for pixels having successful COT/CER retrieval pairs present in either the standard overcast SDSs or the PCL SDSs. For all retrieval channel pairs except 1.6/2.1 μm, pixels with an x-axis VNSWIR reflectance larger than the maximum LUT reflectance (i.e., the green region to the right of the LUT in Fig. 11) are considered successful retrievals with COT set to the maximum allowed value (note that the LUT COT maximum is 158, but the maximum reported value is limited to 150); thus, the RFM SDS for these pixels will contain fill values even though the solutions originate from the ASL routine. For the 1.6-/2.1-μm channel pair, because of substantial cloud particle absorption for the x-axis 1.6-μm reflectance, only the ASL CER retrieval is useful when the reflectance pair is in the green region of the solution space, and is therefore reported in the RFM.

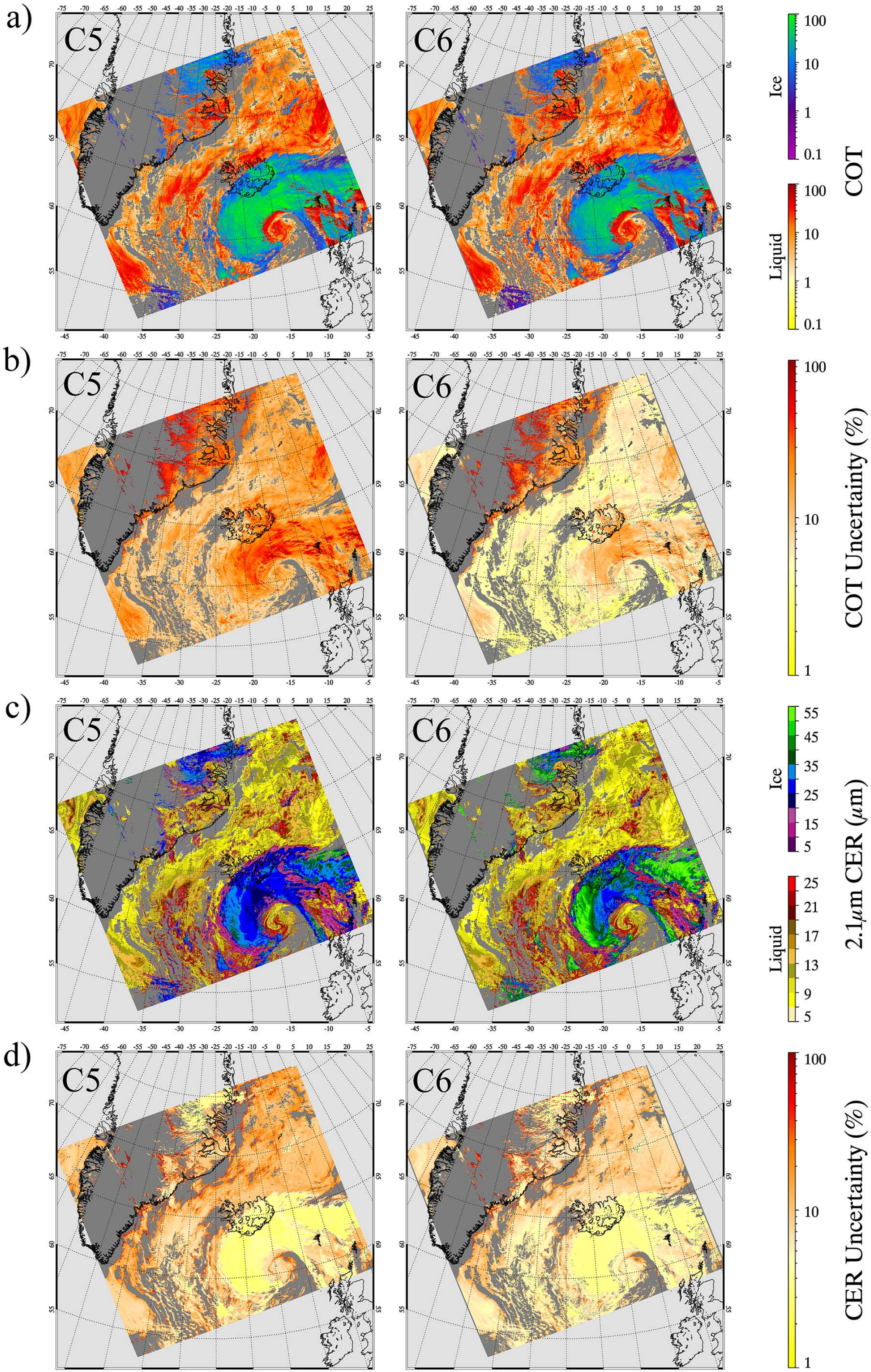

Fig. 12. Retrievals of (a) COT and (b) 2.1-μm CER for an Aqua MODIS data granule over Greenland (July 1, 2008, 1400UTC). The corresponding (c) COT and (d) CER retrieval uncertainties are given. The left and right images in each panel correspond to results from C5 and C6, respectively. For C6, retrieval uncertainties for both COT and 2.1-μm CER decreased compared with C5.

Furthermore, as was previously discussed in Section III-C, each spectral channel pairing has a different rate of retrieval failure [63] due to differences in the absorbing CER wavelengths (e.g., penetration depths, sensitivities to cloud inhomogeneity or 3-D radiative effects, atmospheric transmittance corrections, etc.) [22], [32], [65], and thus the various spectral RFM SDSs should not be expected to contain identical pixel populations.

As an example, RFM statistics were analyzed for overcast pixels from an Aqua MODIS data granule southwest of Baja California on July 2, 2008, 2105 UTC. Comprising tropical storm Douglas, the granule contains a variety of liquid and ice phase clouds over both ocean and land surfaces (browse imagery available at lance.modaps.eosdis.nasa.gov/cgi-bin/imagery/realtime.cgi). Liquid phase CER (2.1 μm) retrieval failure rates corresponding to regions II and III of Fig. 11 were 4% and 11%, respectively. For liquid CER (3.7 μm) retrievals, 6% and 5% of attempted retrievals failed, respectively. Ice phase CER (2.1 μm) retrieval failure rates corresponding to regions II and III were 8% and 3%, respectively, while 6% and 7% of CER (3.7 μm) retrievals failed, respectively. For the global ocean liquid water cloud study reported in [63], there was an overall failure rate of about 16% and 10% for CER (2.1 μm) and CER (3.7 μm) retrievals, respectively; the majority of failures occurred in region III and were more likely to be associated with broken and heterogeneous cloudy scenes.

F. Improved Pixel-Level Retrieval Uncertainty

Estimates of the pixel-level uncertainty (RMS relative uncertainty normalized to percent) in COT, CER, and WP were added in C5 as first described in [24]. The uncertainty estimates are derived by propagating uncertainties applied to component error sources that are inherent to the retrieval. This is done by calculating partial derivative sensitivities (i.e., Jacobians)—for example, of cloud top reflectance with respect to COT at the two channels used in the retrieval, while holding the other parameters (CER, surface spectral reflectance, etc.) constant—coupled with estimates of cloud top reflectance uncertainties associated with each error source. In this way, each error source uncertainty is mapped into cloud top reflectance uncertainty that is then mapped into retrieval uncertainty. The approach allows partial derivatives to be calculated from the radiative transfer LUTs for computational efficiency. For C6, error sources include: 1) instrument calibration; 2) atmospheric corrections; 3) surface spectral reflectance; and 4) other forward model error sources. While not currently part of the reported uncertainty budget, work on flagging, understanding, and perhaps improving 3-D error sources is ongoing.

The mapping of measured and model uncertainty components into retrieval uncertainty is represented by the covariance matrix S_{Ret}, such that

$$\mathbf{S}_{\text{Ret}} = \left(\mathbf{K}^T \mathbf{S}_y^{-1} \mathbf{K}\right) + \sum_i (\mathbf{K}^{-1}\mathbf{K}_{b_i})\mathbf{S}_{b_i}(\mathbf{K}^{-1}\mathbf{K}_{b_i})^T \qquad (4)$$

where $\mathbf{S}_y$ and $\mathbf{S}_b$ are the measurement and model covariance matrices, respectively. The partial derivatives in $\mathbf{K}$ map cloud top reflectance error into retrieval error (e.g., matrix elements $\partial R_\lambda/\partial\tau$ and $\partial R_\lambda/\partial r_e$). For the present two-channel retrieval problem, the matrices are of size 2 × 2. The elements of $\mathbf{K}_b$ contain partial derivatives of reflectance with respect to some channel-dependent model parameter (e.g., spectral surface albedo, spectral above-cloud atmospheric transmittance, etc.); the i-index summation is over each independent model error source. The $\mathbf{K}_b$ matrices are diagonal with the exception of atmospheric transmittance errors due to water vapor uncertainties that affect each channel in a correlated manner. The matrix formulation of (4) can be derived from standard variance algebra, only keeping first-order (linear) terms, and is equivalent to the retrieval error covariance matrix formulation used in optimal estimation retrievals [66] when the *a priori* information is removed (i.e., given large error covariance values).

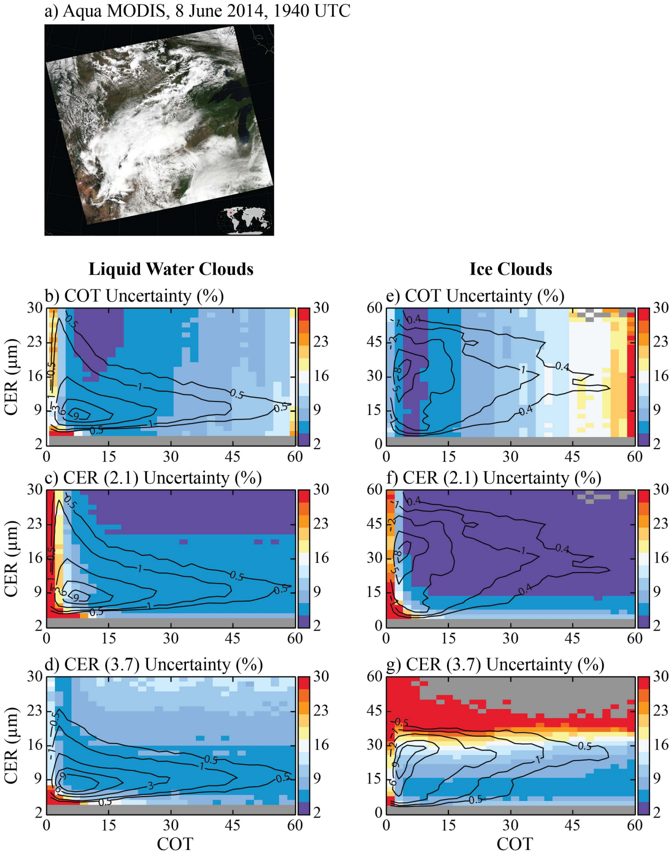

Fig. 13. (a) Total calculated mean liquid water and ice cloud retrieval uncertainties binned as a function of COT and CER for all successful retrievals from the central U.S. granule. (b) and (e) COT uncertainties are relatively higher at small and large COT with sensitivity to CER only for the smallest sizes. (c), (d), (f), and (g) CER uncertainties are generally higher at small COT and CER. Gray-shaded bins either indicate effective radius values outside the LUT or the absence of pixels in the granule with that COT–CER retrieval pair. Contours of normalized retrieval counts for the COT and CER pairs are also shown.

C5 processing assumed the instrument radiometric calibration relative uncertainty was fixed at 5% in all VNIR/SWIR spectral channels [this value was also intended to include nominal uncertainty in cloud forward model error sources that are now partially captured in C6, i.e., items 2) and 3)], the relative uncertainty in water vapor (from NCEP GDAS) used in above-cloud atmospheric corrections was 20%, and the spectral surface albedo uncertainty associated with the MOD43B product was 15% in all spectral channels and in all land locations. In C6 processing, error sources are modified/expanded to include: 1) scene-dependent calibration uncertainty that depends on the channel and detector-specific uncertainty index (UI) provided in the L1B file; 2) new model error sources derived from the LUTs that include sensitivities associated with wind direction and speed over the ocean and

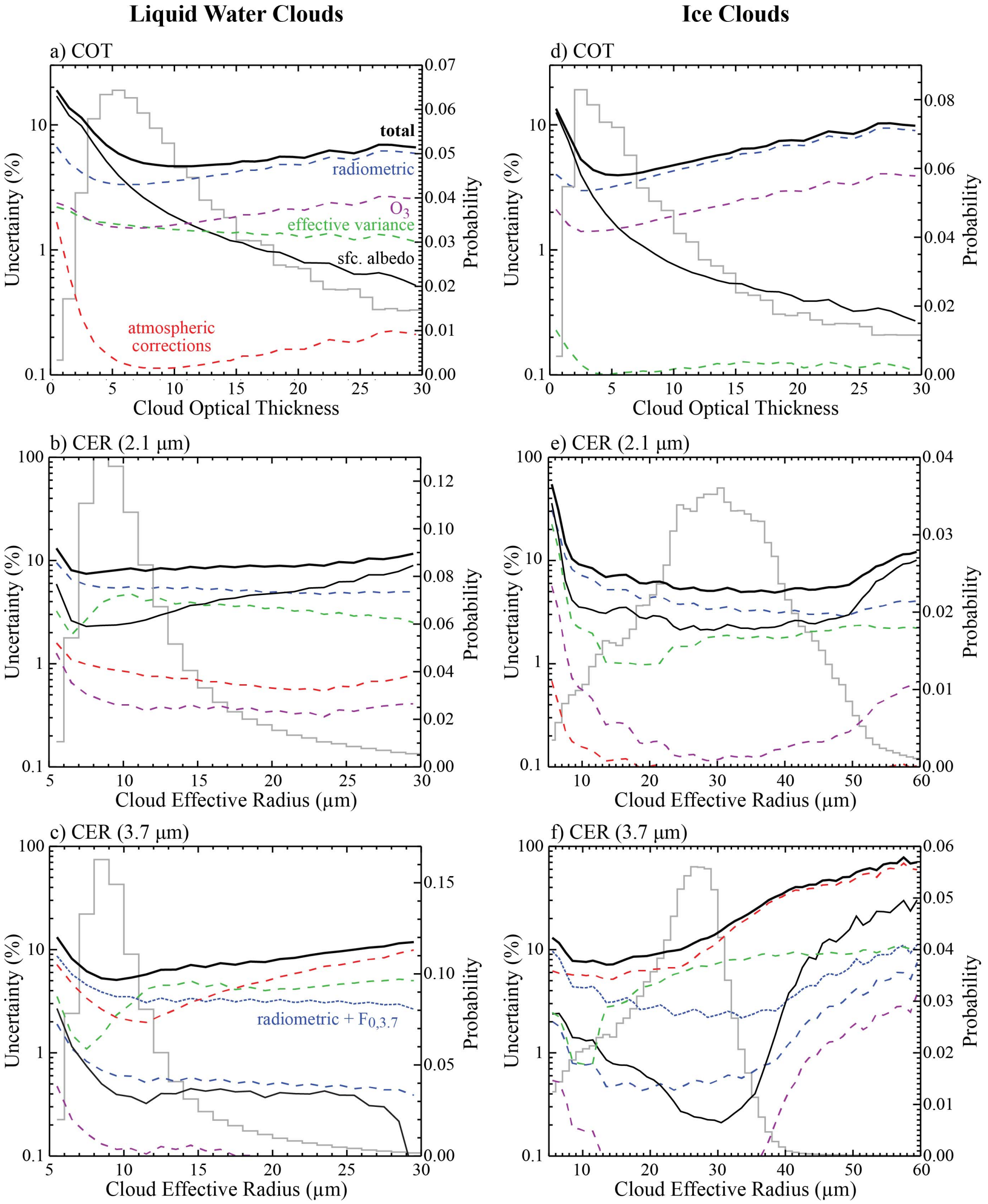

Fig. 14. For the granule of Fig. 13, mean liquid water and ice retrieval uncertainties (left ordinate) as a function of COT or CER for the following error source components: total (i.e., all error sources, thick black line), instrument radiometric uncertainty (blue dashed line) plus uncertainty in 3.7-μm solar spectral irradiance [blue dotted line, (c) and (f) only], surface albedo (thin black), above-cloud atmospheric correction including path transmittance and above-cloud precipitable water errors but excluding O_3 (red dashed line), cloud effective variance (green dashed line), and above-cloud O_3 transmittance correction for the 0.66-μm channel (purple dashed line). See Table IV for details. The retrieval probability distribution (gray line) is shown on the right ordinate of each panel.

uncertainties in liquid and ice size distribution effective variance; 3) thermal emission uncertainties in the 3.7-μm channel associated with cloud and surface temperatures that are needed to extract reflected solar radiation from the total radiance signal; 4) uncertainty in the solar spectral irradiance at 3.7μm; and 5) addition of stratospheric ozone uncertainty in the visible (0.66 μm) atmospheric correction. These source uncertainty assignments used in C6 pixel-level retrieval uncertainty calculations are summarized in Table IV; note that retrieval uncertainties also depend on the solar and view zenith geometry.

With respect to scene-dependent calibration uncertainty, in C6, the L1B pixel-level UI is now used. The UI is an integer value that ranges from 0 to 15 as an indication of relative measurement uncertainty, and is defined such that pixel-level relative uncertainty can be calculated for all MODIS channels via

$$\text{uncertainty}(\%) = \text{specified\_uncertainty} \cdot \exp\left(\frac{\text{UI}}{\text{scale\_factor}}\right) \tag{5}$$

where the values of s*pecified_uncertainty* and s*cale_factor* depend on the spectral channel and are provided in the

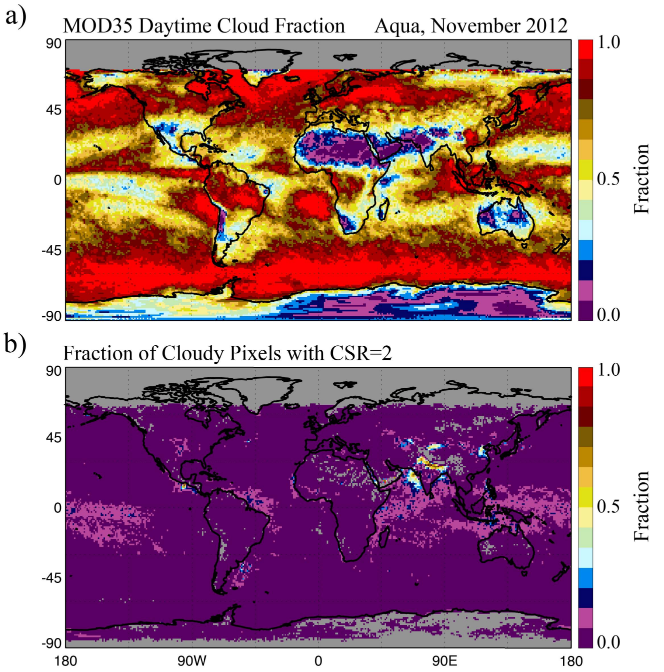

Fig. 15. Aqua MODIS monthly (a) cloud fraction from the MOD35 cloud mask and (b) fraction of cloudy pixels that were identified as “not cloudy” by the MOD06 CSR algorithm (i.e., $\text{CSR} = 2$ designation) for November 2012.

L1B files [41]. With this definition, relative uncertainties range between 1.5% ($\text{UI} = 0$) and 12.8% ($\text{UI} = 15$) for the 0.66- and 0.87-μm channels, between 1.5% and 30% for the 1.24-, 1.6-, and 2.1-μm channels, and between 0.56% and 24% for the 3.7-μm channel. While useful for capturing scene-dependent calibration sensitivities, a minimum allowable relative radiometric uncertainty of 2% is set for the 0.66- and 0.87-μm channels and 3% for the 1.24-, 1.6-, 2.1-, and 3.7-μm channels.

As was the case in C5, the uncertainty in COT over the ocean is typically smallest when the COT lies between 3 and 20, and increases with optical thickness due to saturation in VNIR reflectance and thereby increased sensitivity to error source uncertainties affecting the knowledge of cloud top reflectance. Uncertainty is also larger for small COT due to uncertainty in surface reflectance and atmospheric corrections. In all cases, the contribution of the radiometric uncertainty component to the overall pixel-level uncertainty is much smaller in C6 than what was assumed (5%) in C5. In contrast, the uncertainty in CER over the ocean is largest for small CER (due to atmospheric correction and calibration uncertainty) and at large CER (due to surface reflectance uncertainty).

Fig. 12 shows C5 and C6 retrievals of (a) COT and (c) 2.1-μm CER for an Aqua MODIS granule over Greenland and nearby ocean where clouds overlie sea ice (July 1, 2008, 1400UTC); the corresponding COT and CER retrieval uncertainties are shown in Fig. 12(b) and (d), respectively. This example highlights the pixel-level uncertainties over land, ocean, and ice surfaces, and for a wide variety of optical properties and phase. Note that the C6 retrieval uncertainties are smaller than those of C5 and in the case of COT are notably smaller. While this result may seem counterintuitive given that more error sources are considered in C6, it is explained by the use of significantly smaller radiometric uncertainties compared with C5. Note again that the previous high value of 5% was meant as a pragmatic approach in C5 to account for 3-D radiative transfer uncertainties that could not be expressed explicitly and are still not part of the model error in C6.

Two-dimensional retrieval uncertainty distribution calculations for liquid water and ice pixels are shown in Fig. 13 for (b) and (e) COT and CER from the (c) and (f) 2.1- and (d) and (g) 3.7-μm channels for an Aqua MODIS data granule over the central U.S. (June 8, 2014, 1940UTC); the true-color RGB image for the granule is shown in (a). All successful retrievals from the “overcast” pixel population (i.e., $\text{CSR} = 0$) are included in the distribution, and therefore a variety of view angles are also included. As expected, based on the shape of the COT and CER solution space (see Fig. 11), the largest COT uncertainties occur at small and large COT where the solution space contours are most closely spaced and with more sensitivity to CER at the smaller sizes. The largest CER uncertainties tend to occur at the smaller COTs before the SWIR/MWIR reflectances asymptote; however, 3.7-μm CER uncertainties also peak at larger CER due to a greater atmospheric correction (transmittance and emission) relative to the correspondingly smaller reflectances. Contours of normalized retrieval counts for the COT and CER pairs are also shown. The location of the retrieval distribution maximum is generally well away from the maximum uncertainty regions. To better appreciate the relative contribution of individual error source components, Fig. 14 shows mean binned liquid water and ice cloud retrieval uncertainties corresponding to the main error sources for (a) and (d) COT and CER from the (b) and (e) 2.1- and (c) and (f) 3.7-μm channels as a function of a single parameter (COT or CER). In addition to the total retrieval uncertainty (thick black line), error source components include instrument radiometric uncertainty (blue dashed line) plus uncertainty in 3.7-μm solar spectral irradiance [dotted blue line for (c) and (f) only], surface albedo (thin black line), above-cloud atmospheric correction including path transmittance and above-cloud precipitable water errors but excluding O_3 (red dashed line), cloud model effective variance (green dashed line), and above-cloud O_3 transmittance correction for the 0.66-μm channel (purple dashed line). Further details are given in Table IV. Though O_3 has no impact on the 2.1-μm channel atmospheric transmittance, the stronger influence of that error source for small 2.1-μm CER uncertainties is because many of the smaller CER retrievals correlate closely with small COT [Fig. 13(c) and (f)]. At the smaller COT, the solution space becomes quite compressed and potentially nonunique for small CER (e.g., Fig. 11). In contrast, for the 3.7-μm uncertainty plots, the solution space is more orthogonal and there is less sensitivity to COT [13]. The retrieval probability distribution (gray line) is shown on the right ordinate of each panel, showing that the COT and CER modes roughly correspond to a minimum in the total uncertainty curve for this example granule.

The significance of Figs. 11–13 is that asking for a single metric for the optical retrieval uncertainty is an ill-posed question. The answer unequivocally depends on numerous

TABLE IV

C6 PIXEL-LEVEL ERROR SOURCES AND ASSOCIATED UNCERTAINTY BOUNDS

Category		Error Source	Specification
Ancillary Data (Related to Surface Reflectance)			
	Land/Snow	MODIS-derived $A_{sfc}(\lambda)$ from MCD43B3	±15% of $A_{sfc}(\lambda)$
	Ocean/Water	surface wind speed	±20% surface wind speed
Above-Cloud Atmospheric Corrections			
	Water Vapor (all channels)	above-cloud ancillary precipitable water (PW)	±20%
		above-cloud atmospheric transmittance LUT	provided in spectral transmittance LUT, derived from profile variances
	O_3 (0.66μm channel)	analytic transmittance formula	±20%
Observations		measurement relative error	max. of L1B Uncertainty Index value or 2% (channels 1-4) and 3% (channels 5-7)
Model		cloud model error from analytic gamma size distribution effective variance (v_e)	standard deviation from v_e=0.05 to 0.2 (0.1 nominal) for both liquid and ice LUTs
		water surface reflectance model error from using Cox-Munk reflectances averaged over wind direction	standard deviation of 4 vector wind directions
3.7μm Cloud Reflectance and Cloud/Surface Emission			
	Cloud Emission (ΔT_c)	ΔP_c (CO_2 slicing retrieval)	±50mb
		ΔPW (IR window retrieval)	±20%
	Surface Emission (ΔT_{sfc})	ΔT_{sfc} (ancillary)	±1K
	Solar Spectral Irradiance (ΔF_0)	$\Delta F_0/F_0$ (reflectance calculation)	~4% ($0.42 W\cdot m^{-2}\cdot \mu m^{-1}$)

factors such as surface type, solar and viewing geometry, atmospheric state, surface and cloud temperature (3.7 μm), and most importantly the location of the retrieval solution within the COT and CER solution space. Moreover, these uncertainty estimates should be considered a baseline, or minimum, uncertainty to the extent that error sources such as 3-D radiative effects are not included in the analysis.

IV. IMPACTS ON GLOBAL STATISTICS

The above C6 updates have had a profound impact on the global cloud optical and microphysical property statistics derived from the MOD06 retrievals. Here, these impacts are discussed via comparisons of the C5 and C6 spatially aggregated global L3 product (MOD08) that provides scalar statistics and 1-D and 2-D histograms on a 1° equal-angle grid for daily (D3), eight-day (E3), and monthly (M3) time periods. The MOD08 product itself has been updated for C6, and now includes statistics for the pixel population identified as PCL by the CSR algorithm (i.e., pixels with CSR = 1 and 3 designations, see Section III-D) along with separate aggregations for COT and CER retrievals from channel pairs using the 1.6- and 3.7-μm channels (see Section III-C). Here, monthly statistics derived from the daily MOD08_D3 and obtained directly from the monthly MOD08_M3 aggregations are shown, namely, for Aqua MODIS during November 2012. Note that the present discussion is intended to provide only a general overview of the statistical impacts of the C6 MOD06 updates; a more detailed analysis of C6 L3 statistics is left for future efforts.

The November 2012 monthly cloud fraction, derived from pixel-weighted daily MOD08_D3 aggregations of the MOD35 cloud mask, is shown in Fig. 15(a). The fraction of the MOD35 cloudy pixels identified as "not cloudy" by the MOD06 CSR algorithm (i.e., CSR = 2 designation, see Section III-D) is shown in (b), and is derived here from MOD08_D3 daily aggregations of the CSR results. Because MOD35 is designed to identify obstructed, i.e., "not clear," pixels, in some regions, the MOD35 cloud fraction may in fact be overestimated as it may incorrectly identify optically thicker aerosols (e.g., dust and smoke) or strong sunglint as clouds. For November 2012, the CSR algorithm identified a large fraction of the MOD35 cloudy pixel population as "not cloudy" over the Indo-Gangetic Plain in northern India, a region known to suffer persistent air pollution [67]–[69] and that for this month was observed by the MOD04 Dark Target aerosol product to have a large monthly mean AOD (not shown), as well as over the relatively cloud-free portion of the northern Arabian Sea where sunglint conditions are commonly encountered. A

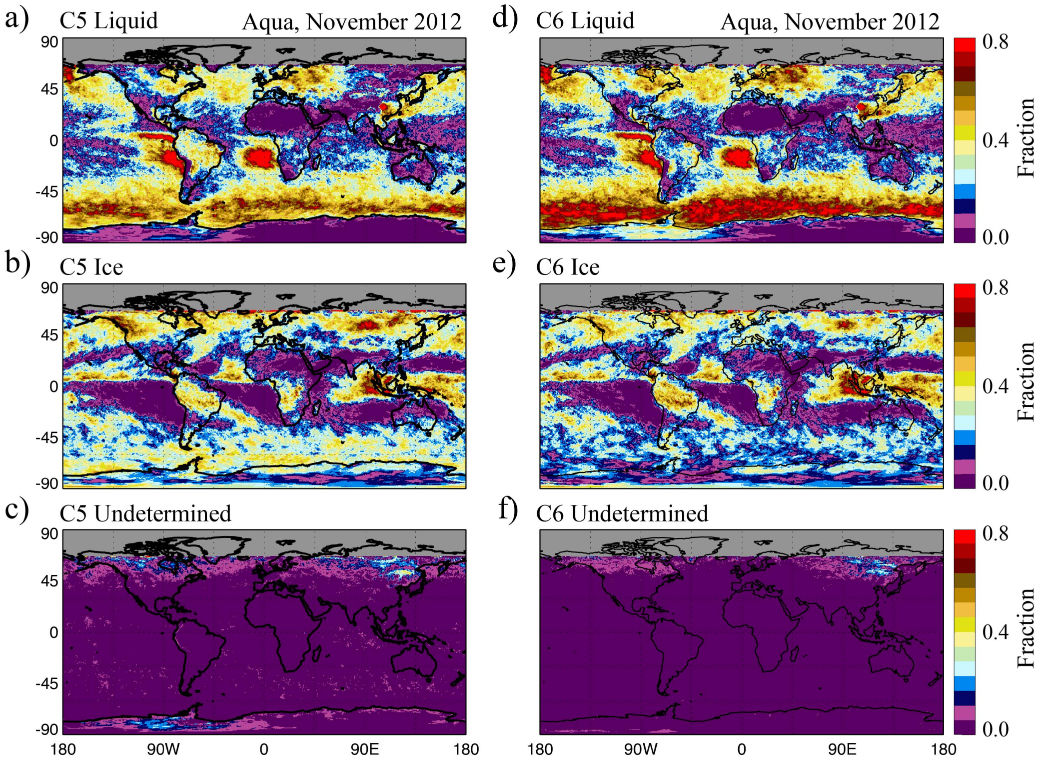

Fig. 16. November 2012 Aqua MODIS monthly cloud fraction (CSR = 0), by COP phase algorithm designation, for C5 (a) liquid, (b) ice, and (c) undetermined phase, and C6 (d) liquid, (e) ice, and (f) undetermined phase.

small fraction of the MOD35 cloudy pixels in low cloud fraction regions over the tropical oceans are also identified as "not cloudy" by the CSR algorithm, again likely due to sunglint (potentially in combination with small broken clouds).

For cloud optical and microphysical property retrievals, the MOD08 statistical aggregations are performed separately by cloud thermodynamic phase. Improvements to the COP thermodynamic phase algorithm for C6 have yielded substantial changes to the liquid, ice, and undetermined pixel populations with respect to C5. These changes are readily seen in the November 2012 monthly cloud phase fraction plots shown in Fig. 16. The C5 liquid, ice, and undetermined phase fractions are shown in (a)–(c), respectively; C6 phase fractions are shown in (d)–(f), respectively. Both the C5 and C6 fractions are calculated directly from the pixel-level MOD06 product using a research-level aggregation code. The phase fraction is defined here as the fraction of total (clear plus cloudy) pixels identified as "overcast" cloudy by the CSR algorithm (CSR = 0 designation) and either liquid, ice, or undetermined phase by the COP phase algorithm; note that these fractions include cloudy pixels regardless of the success of the cloud optical and microphysical retrievals, and thus are different from the cloud retrieval fractions that are the respective fractions of total pixels having successful liquid, ice, or undetermined retrievals. First, it is evident that the C6 COP phase algorithm identifies a significantly larger fraction of liquid phase clouds than does C5, in particular over the southern oceans, roughly below latitude 45 °S. This regional increase in liquid phase fraction for C6 is accompanied by a regional decrease in ice phase fraction. Also note that the C6 undetermined phase fraction has decreased compared with C5; further analysis (not shown here) reveals that most of this decrease is the result of C5 undetermined phase pixels being identified (and validated) as liquid phase in C6 [61].

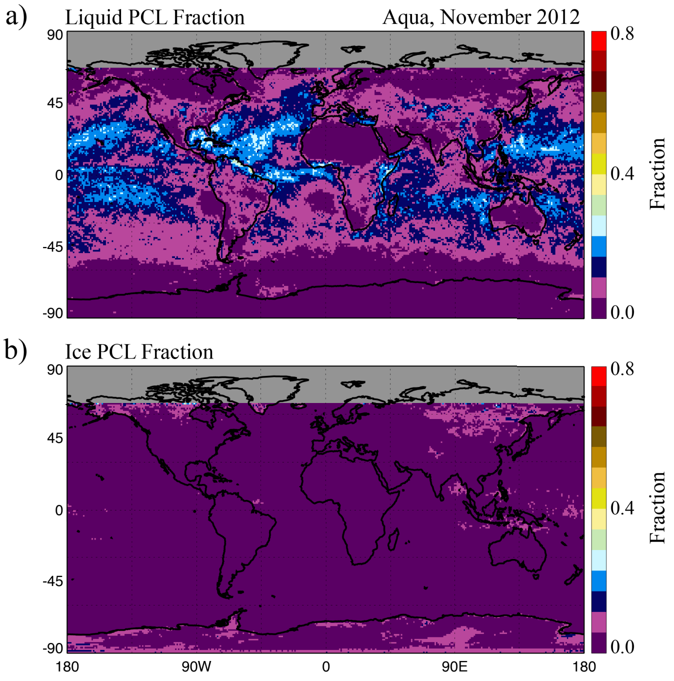

Fig. 17. November 2012 Aqua MODIS monthly (a) liquid and (b) ice cloud fraction for the PCL pixel population (CSR = 1 and 3 designations).

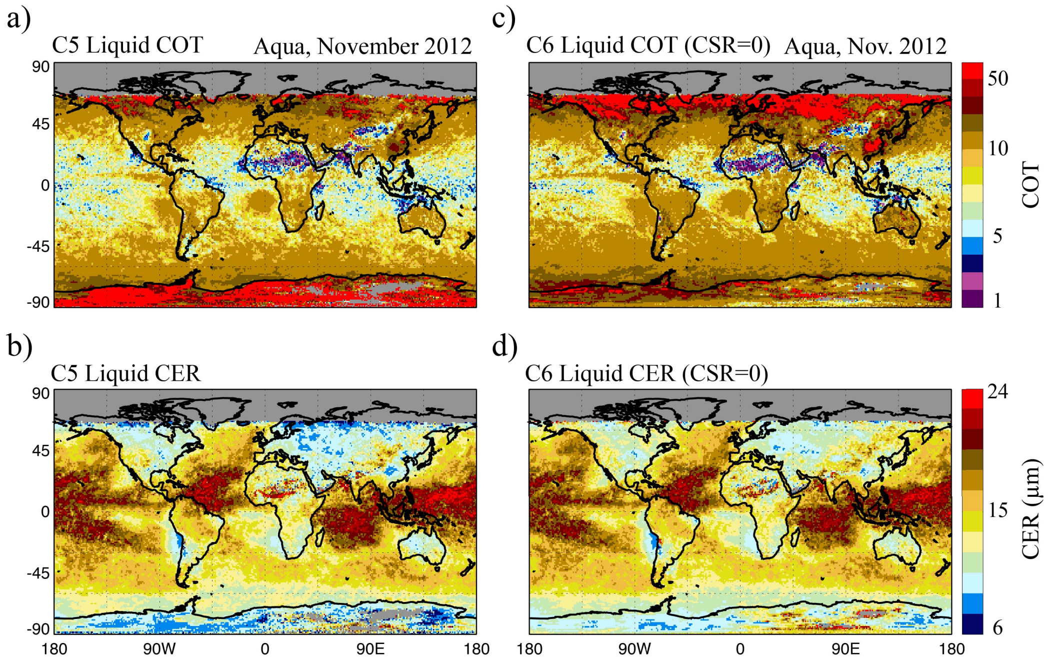

Fig. 18. November 2012 Aqua MODIS monthly mean liquid phase COT and CER, using the channel combination that includes 2.1 μm, for C5 [(a) and (b), respectively] and C6 [(c) and (d), respectively]. To remain consistent with the C5 MOD06 decision to report only those retrievals identified as "overcast" by the CSR algorithm (CSR = 0 designation), the C6 means shown here are for the CSR = 0 pixel population only.

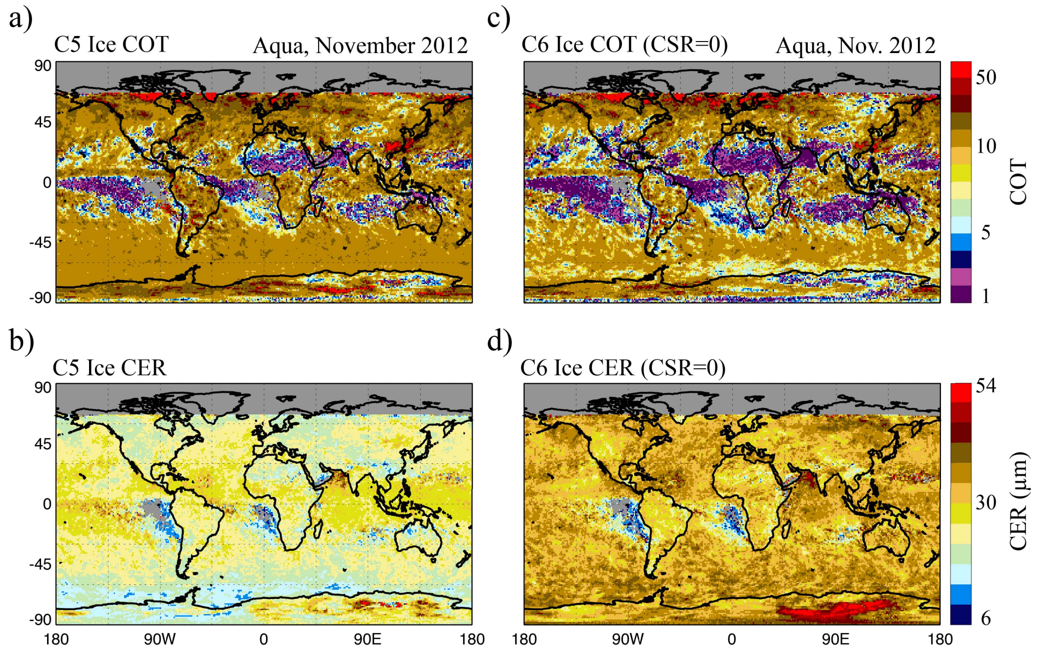

Fig. 19. Same as Fig. 18, except for ice phase clouds.

Fig. 17 shows C6 monthly (a) liquid and (b) ice phase fractions for the PCL pixel population (CSR = 1 and 3 designations). Similar to Fig. 16, these fractions include cloudy pixels regardless of the success of the cloud optical and microphysical retrievals. First note that, for this month, the ice phase PCL pixel population is small, with fractions generally less than a few percent. The liquid phase PCL fraction, on the other hand, is much larger, with values approaching 20% or more. The liquid phase PCL fraction maxima are primarily located in regions where the cloud fraction (Fig. 15) is smaller, i.e., more broken cloud regimes, in particular over the ocean due to the PCL CSR = 3 test; note that this test, which uses the MOD35 250-m subpixel cloudiness flags, is only applied over water surfaces.

The changes in the liquid and ice phase pixel populations shown in Fig. 16 will in turn impact the monthly cloud optical and microphysical retrieval statistics. Monthly mean liquid phase COT and CER for November 2012, using the channel

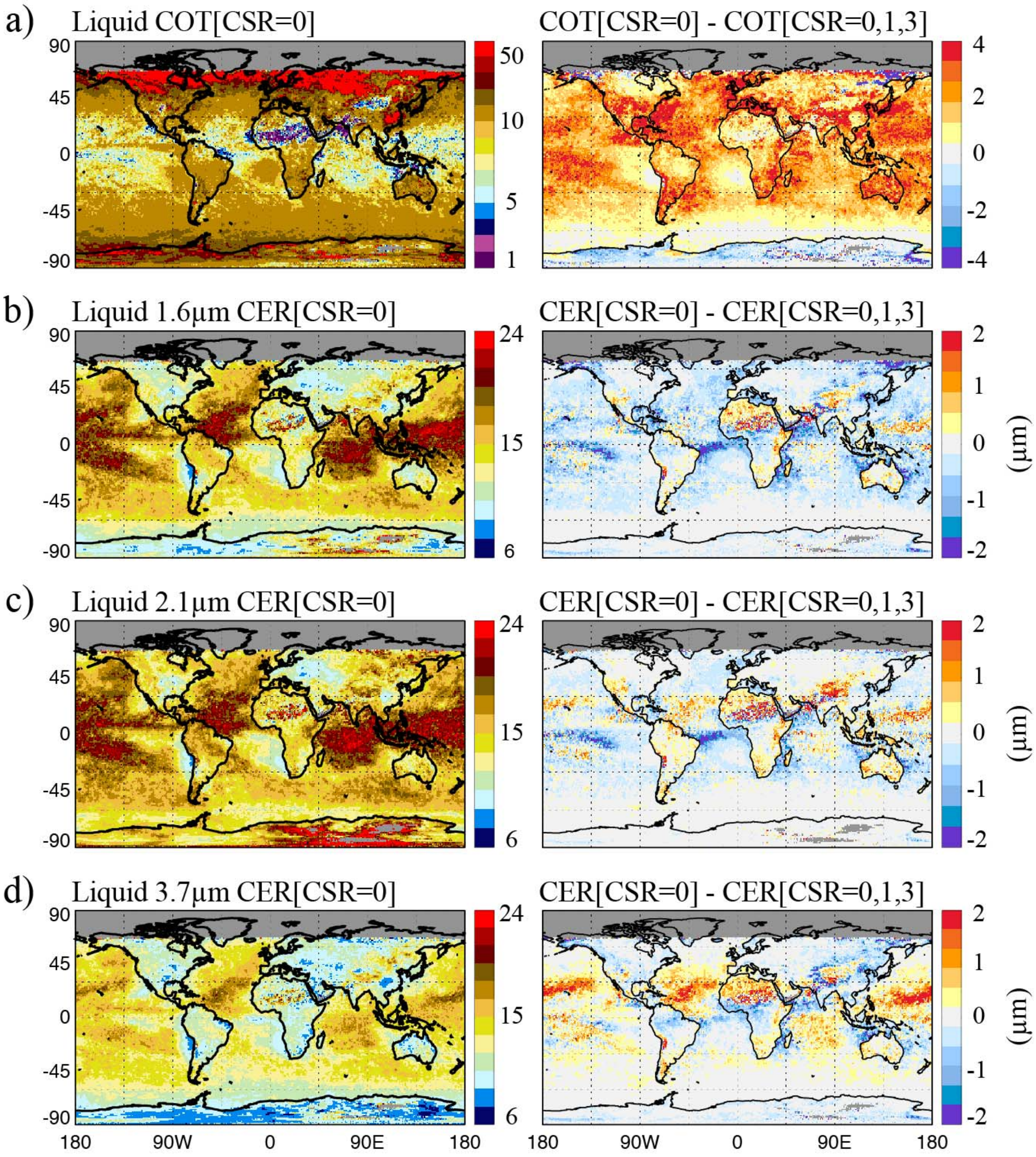

Fig. 20. November 2012 Aqua MODIS monthly mean liquid phase (a) COT and CER from the (b) 1.6-, (c) 2.1-, and (d) 3.7-μm wavelength channels for the “overcast” CSR = 0 pixel population. Note that the C5 MOD06 cloud optical and microphysical properties were reported only for this pixel population. The impacts of excluding the PCL pixel population (CSR = 1 and 3 designations) in calculations of the monthly mean COT and spectral CER retrievals are shown in the right column.

combination that includes 2.1 μm, are shown in Fig. 18 for C5 [(a) and (b), respectively] and C6 [(c) and (d), respectively]. Note that the C6 pixel population is limited here to those pixels identified as “overcast” by the CSR algorithm (CSR = 0 designation) to remain consistent with the C5 MOD06 decision to report retrievals only for those pixels having CSR = 0; these means are directly obtained from the MOD08_M3 monthly product. While the monthly mean liquid phase CER between C5 and C6 appears relatively consistent, the monthly mean liquid phase COT is generally larger in C6 than in C5, in particular over the southern oceans where the largest changes in cloud phase identification occurred (increased C6 liquid phase fraction, see Fig. 16) as well as across the high northern latitudes. Also note that a decrease in monthly mean liquid phase COT for C6 is observed over Antarctica, again possibly due to an increase in liquid phase fraction, though in this region, the cloud fractions are generally small.

For ice phase clouds, in addition to the change in pixel population, the new ice crystal radiative model for C6 (i.e., severely roughened aggregated columns) will also impact the monthly retrieval statistics, namely, by yielding smaller COT, due to a smaller asymmetry factor for C6, as well as larger CER from the 2.1-μm wavelength channel, due to a smaller coalbedo (see Section III-A). Monthly mean ice phase COT and CER for November 2012, using the channel combination that includes 2.1 μm, are shown in Fig. 19 for C5 [(a) and (b), respectively] and C6 [(c) and (d), respectively]. The C6 pixel population is again limited to those pixels identified as “overcast” by the CSR algorithm (CSR = 0 designation), and all means are obtained directly from the MOD08_M3 monthly product. Disregarding ice phase pixel population differences, the monthly mean COT for C6 is smaller than

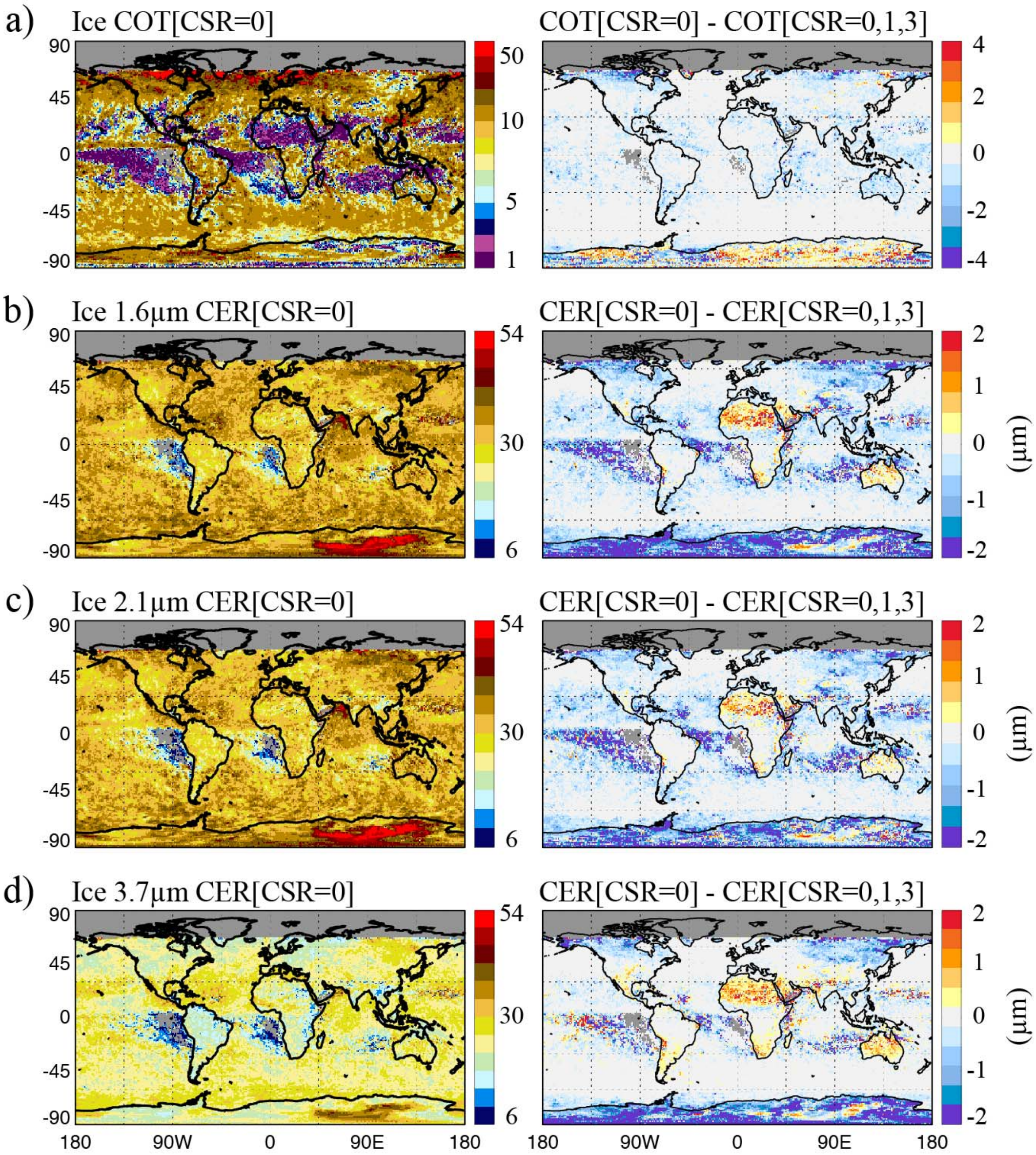

Fig. 21. Same as Fig. 20, except for ice phase clouds.

for C5, and the monthly mean CER is larger, as expected due to the changes in the assumed ice crystal SS properties.

The impact of excluding the PCL pixel population (CSR = 1 and 3 designations) on monthly liquid phase COT and CER means, as was previously done in C5, is shown in Fig. 20. Here, the monthly mean liquid phase (a) COT and spectral CER from the (b) 1.6-, (c) 2.1-, and (d) 3.7-μm wavelength channels are shown in the left column for the "overcast" CSR = 0 population. The respective differences between monthly means of the CSR = 0 pixel population and the entire liquid cloud pixel population (CSR = 0, 1, and 3 designations) are shown in the right column; the differences are defined here such that a monthly mean increase (decrease) when excluding PCL pixels is identified by warmer (cooler) colors. With the exception of Antarctica, as well as the stratocumulus regions of the southwest coasts of Africa and South America where the liquid phase PCL fraction is low (see Fig. 17), it is evident here that excluding the PCL pixels in the calculation of monthly mean liquid phase COT yields larger mean COT, with absolute differences in some regions of up to two or more. This result for COT is expected, given that the PCL pixel population is presumably composed of heterogeneous broken cloudy or cloud edge pixels. The spectral CER differences, on the other hand, are more mixed with regions of high liquid cloud fraction (see Fig. 16) exhibiting little to no difference in mean CER and regions with low liquid cloud fraction (i.e., more broken cloud regimes) having either increased or decreased mean CER when excluding the PCL pixels.

The impact of excluding the PCL pixel population on monthly mean ice phase COT for the three primary spectral CER retrievals is shown in Fig. 21. Similar to Fig. 20, the monthly mean ice phase (a) COT and spectral CER from the (b) 1.6-, (c) 2.1-, and (d) 3.7-μm wavelength channels are shown in the left column for the "overcast" CSR = 0 population, and the respective differences between monthly means of the CSR = 0 pixel population and the entire ice cloud pixel population (CSR = 0, 1, and 3 designations) are shown in the right column. Unlike the liquid phase mean, monthly mean ice phase COT is generally unchanged, or in some regions is only slightly smaller (absolute differences less than one), when excluding the PCL pixels. The exception is over Antarctica, where mean COT generally increases when excluding PCL pixels. A more discernable pattern is also exhibited by the ice phase spectral CER monthly means, as regions of higher ice cloud fraction show little to no difference, and regions of lower ice cloud fraction over ocean and land have smaller and larger mean CER, respectively, when excluding the PCL pixels. Again, the exception is over Antarctica, where monthly mean CER from all three spectral channels is generally smaller when excluding the PCL pixels.

Finally, as previously mentioned (Section II), a new L1B reaggregation scheme has been applied to Aqua MODIS Atmosphere Team C6 processing to help ameliorate a known focal plane misalignment between the two 250-m resolution channels (0.66 and 0.87 μm) and the 500-m resolution channels (0.47, 0.55, 1.24, 1.6, and 2.1 μm). This reaggregation had notable effects on COT and CER statistics in broken low cloud regimes (not shown), though the effects are generally much smaller than those of the other C6 algorithm updates discussed in Section III. Liquid water cloud retrieval fractions increase slightly over the ocean, up by as much as 0.02–0.5 in some regions. COT decreased somewhat, by about two over many ocean and land regions. CER changes were both positive (e.g., $+2$ μm in tropical Atlantic and Pacific and broadly over many land masses) and negative (-1 μm in marine stratocumulus regimes).

V. SUMMARY AND CONCLUSION

Many updates to the C6 MOD06 cloud optical and microphysical property product were introduced to provide additional information previously not available in C5, such as separately reporting cloud CER retrievals from three absorbing spectral channels (1.6, 2.1, and 3.7 μm), reporting retrievals for pixels identified as either PCL or at cloud edge by the CSR algorithm, and reporting information to diagnose retrieval failures. However, such additional information may lead to confusion or erroneous conclusions if interpreted improperly. Here, best-practice guidance is provided for appropriate interpretation and usage of several key features of the C6 MOD06 cloud optical and microphysical property product.

A. Retrieval Quality

Previously in C5, the quality of the cloud optical and microphysical retrievals was provided in part by a confidence QA bit flag (values from zero for no confidence to three for high confidence) within the *Quality_Assurance_1km* SDS, as well as the pixel-level retrieval uncertainty. In C6, however, the confidence QA is now set to three (i.e., high confidence) for all successful retrievals such that it is no longer useful for quality assessment. Nevertheless, sufficient information is provided in accompanying SDSs for users to infer retrieval quality.

Because large pixel-level retrieval uncertainty implies that the reflectance observations lie in a portion of the LUT solution space that is less sensitive to the retrieved quantity, users are advised to determine retrieval quality in part via retrieval uncertainty; note that the maximum reported retrieval uncertainty for all optical and microphysical quantities is 200%. However, uncertainties on the order of 50% might be expected to be of little value for science analysis since the calculations are considered to give a baseline (minimum) uncertainty due to error sources not included and also due to the linear assumption inherent in the calculations (4). Users are also encouraged to look at the subpixel heterogeneity index [28] reported in the new *Cloud_Mask_SPI* SDS that provides a measure of scene variability within each 1-km pixel. Large subpixel heterogeneity has been shown to be associated with retrieval biases [22], [32] and increased retrieval failure rates [63]. Likewise, users can also query the *Cloud_Multi_Layer_Flag* SDS in conjunction with the *Quality_Assurance_1km* SDS, as multilayer cloud scenes are problematic for retrievals such as MOD06 that assume a single cloud layer and phase. A full description of the individual bit settings in the QA SDS is provided as an SDS attribute in every MOD06 file. Users should check the sixth byte of the QA for the results of the individual multilayer cloud tests, and are currently advised to exclude multilayer pixel detection when only the PH test is triggered due to false positives produced for moderately thick single layer ice clouds (see Section III-D).

Finally, in some instances, the cloud top retrievals may fail, e.g., due to known saturation issues with the 14-μm CO_2-slicing channel. In these cases, the MOD06 optical and microphysical retrievals default to the surface temperature and pressure for the cloud top assumption and atmospheric corrections, thus yielding suspect retrievals. Users are advised to discard MOD06 optical and microphysical retrievals that have corresponding 1-km CTT or pressure retrievals set to fill values.

B. Interpreting the Spectral Microphysical Retrievals

While the three absorbing spectral channels used to retrieve CER have been shown to have different penetration depths within a plane-parallel vertically inhomogeneous cloud [70], users should nevertheless be cautious drawing conclusions from CER retrieval differences, e.g., inferring vertical cloud droplet size distributions. Horizontal heterogeneity has also been shown to impact spectral CER retrievals differently [32], [22]. Errors in atmospheric corrections, the 3.7-μm emission correction, etc., may yield artifacts in the spectral CER differences. In addition, 1.6-μm CER retrievals from Aqua MODIS require greater scrutiny due to known nonfunctioning detectors and potential unknown issues with the remaining functional detectors.

C. Using PCL Retrievals

As discussed in Section III-D, retrievals of pixels identified as either PCL or at cloud edge are now reported in C6, whereas they were discarded in C5. Caution should nevertheless be exercised when using these PCL retrievals. It has been shown that PCL pixels have the highest rates of cloud optical and microphysical retrieval failure, as roughly 34% of attempted retrievals of global over-ocean liquid phase PCL pixels using the VNSWIR-2.1 μm channel pair failed, compared with a failure rate of roughly 10% for overcast CSR = 0 pixels [63]. This result implies a likely failure in the homogeneous 1-D plane-parallel cloud radiative model, and gives some credence to the C5 approach of discarding all PCL pixels. Furthermore, subpixel cloud heterogeneity has also been shown to cause CER retrieval biases, as well as artificial differences in spectral CER retrievals [22], [32].

D. Interpreting the Retrieval Failure Metric

The RFM represents an attempt to provide additional information about COT and CER retrieval failures, specifically the LUT COT and CER values nearest to the observed reflectances (when applicable) and a CM that provides a measure of the "degree of failure," i.e., the relative distance of the observed reflectances from the LUT solution space. The RFM COT, CER, and CM parameters are assigned values such that the user can ascertain how a given spectral retrieval failed (see Fig. 11 and Table III). While smaller CM values do indicate that the observed reflectances may be close to the LUT solution space, and thus indicate a greater confidence in the RFM COT and CER values, users are nevertheless cautioned against quantitatively using this data, e.g., for process studies.

While this paper is intended as a resource for users of the C6 MODIS cloud optical properties products, as an overview document, it is necessarily limited to succinct summaries of major C6 changes and results. Additional details on all aspects of C6 MOD06/MYD06 optical property algorithms, data sets, quality assessment information, format, content, and best practices are available in the online cloud optical property C6 user guide posted to the MODIS Atmosphere Team Web site [71]. The user guide also provides information on associated sampled (MODATML2/MYDATML2) and gridded L3 (MOD08/MYD08) data sets. All users are encouraged to consult the guide for further information.

ACKNOWLEDGMENT

The authors would like to thank E. Masuoka, MODIS Adaptive Processing System lead, and his team for enabling extensive product testing during C6 algorithm development, in particular V. S. Manoharan for MODIS Atmosphere Team quality assessment support and X. (Jack) Xiong and his MODIS Characterization and Support Team for providing critical support in quantifying MODIS reflectance radiometric uncertainties. They would also like to thank S. A. Ackerman, R. Frey, and B. A. Baum for many helpful discussions regarding the C6 cloud masking and cloud top property products, as well as L. Oreopoulos, T. Fauchez, and L. Di Girolamo for helpful feedback. All MODIS data used here are publically available from the NASA Land and Atmospheres Archive and Distribution System at ladsweb.nascom.nasa.gov/data/; DOI information for the C6 cloud product is given in [5].

REFERENCES

[1] V. V. Salomonson, W. Barnes, P. W. Maymon, H. E. Montgomery, and H. Ostrow, "MODIS: Advanced facility instrument for studies of the Earth as a system," *IEEE Trans. Geosci. Remote Sens.*, vol. 27, no. 2, pp. 145–153, Mar. 1989.

[2] M. D. King, Y. J. Kaufman, W. P. Menzel, and D. Tanré, "Remote sensing of cloud, aerosol, and water vapor properties from the Moderate Resolution Imaging Spectrometer (MODIS)," *IEEE Trans. Geosci. Remote Sens.*, vol. 30, no. 1, pp. 2–27, Jan. 1992.

[3] C. O. Justice *et al.*, "An overview of MODIS land data processing and product status," *Remote Sens. Environ.*, vol. 83, nos. 1–2, pp. 3–15, Nov. 2002.

[4] W. E. Esaias *et al.*, "An overview of MODIS capabilities for ocean science observations," *IEEE Trans. Geosci. Remote Sens.*, vol. 36, no. 4, pp. 1250–1265, Jul. 1998.

[5] S. Platnick *et al.* (2015). MODIS atmosphere L2 cloud product (06_L2). NASA MODIS Adaptive Processing System, Goddard Space Flight Center, Greenbelt, MD, USA. [Online]. Available: http://dx.doi.org/10.5067/MODIS/MOD06_L2.006

[6] S. Platnick *et al.*, "The MODIS cloud products: Algorithms and examples from Terra," *IEEE Trans. Geosci. Remote Sens.*, vol. 41, no. 2, pp. 459–473, Feb. 2003.

[7] W. P. Menzel *et al.*, "MODIS global cloud-top pressure and amount estimation: Algorithm description and results," *J. Appl. Meteorol. Climatol.*, vol. 47, no. 4, pp. 1175–1198, Apr. 2008.

[8] B. A. Baum *et al.*, "MODIS cloud-top property refinements for collection 6," *J. Appl. Meteorol. Climatol.*, vol. 51, no. 6, pp. 1145–1163, Jun. 2012.

[9] D. P. Wylie and W. P. Menzel, "Eight years of high cloud statistics using HIRS," *J. Clim.*, vol. 12, no. 1, pp. 170–184, Jan. 1999.

[10] T. Nakajima and M. D. King, "Determination of the optical thickness and effective particle radius of clouds from reflected solar radiation measurements. Part I: Theory," *J. Atmos. Sci.*, vol. 47, no. 15, pp. 1878–1893, Aug. 1990.

[11] S. Platnick and S. Twomey, "Determining the susceptibility of cloud albedo to changes in droplet concentration with the advanced very high resolution radiometer," *J. Appl. Meteorol.*, vol. 33, no. 3, pp. 334–347, Mar. 1994.

[12] S. Platnick and F. P. J. Valero, "A validation of a satellite cloud retrieval during ASTEX," *J. Atmos. Sci.*, vol. 52, no. 16, pp. 2985–3001, Aug. 1995.

[13] S. Platnick, J. Li, M. D. King, H. Gerber, and P. V. Hobbs, "A solar reflectance method for retrieving the optical thickness and droplet size of liquid water clouds over snow and ice surfaces," *J. Geophys. Res.*, vol. 106, no. D14, pp. 15185–15199, Jul. 2001.

[14] M. D. King *et al.*, "Remote sensing of liquid water and ice cloud optical thickness and effective radius in the arctic: Application of airborne multispectral MAS data," *J. Atmos. Ocean. Technol.*, vol. 21, no. 6, pp. 857–875, Jun. 2004.

[15] M. D. King *et al.* (2008). Collection 005 change summary for the MODIS cloud optical proper-ties (06_OD) algorithm. NASA Goddard Space Flight Center, Greenbelt, MD, USA. [Online]. Available: http://modis-atmos.gsfc.nasa.gov/_docs/C005CloudOpticalPropertiesver3.3.pdf

[16] M. D. King, S. C. Tsay, S. E. Platnick, M. Wang, and K. N. Liou. (1997). Cloud retrieval algorithms for MODIS: Optical thickness, effective particle radius, and thermodynamic phase. NASA Goddard Space Flight Center, Greenbelt, MD, USA. [Online]. Available: http://modis-atmos.gsfc.nasa.gov/_docs/atbd_mod05.pdf

[17] M. D. King *et al.*, "Cloud and aerosol properties, precipitable water, and profiles of temperature and water vapor from MODIS," *IEEE Trans. Geosci. Remote Sens.*, vol. 41, no. 2, pp. 442–458, Feb. 2003.

[18] B. A. Baum *et al.*, "Bulk scattering properties for the remote sensing of ice clouds. Part II: Narrowband models," *J. Appl. Meteorol.*, vol. 44, no. 12, pp. 1896–1911, Dec. 2005.

[19] P. Yang *et al.*, "Differences between collection 4 and 5 MODIS ice cloud optical/microphysical products and their impact on radiative forcing simulations," *IEEE Trans. Geosci. Remote Sens.*, vol. 45, no. 9, pp. 2886–2899, Sep. 2007.

[20] G. Wind *et al.*, "Multilayer cloud detection with the MODIS near-infrared water vapor absorption band," *J. Appl. Meteorol. Climatol.*, vol. 49, no. 11, pp. 2315–2333, Nov. 2010.

[21] J. A. Joiner, P. Vasilkov, P. K, Bhartia, G. Wind, S. Platnick, and W. P. Menzel, "Detection of multi-layer and vertically-extended clouds using A-Train sensors," *Atmos. Meas. Techn.*, vol. 3, pp. 233–247, 2010.

[22] Z. Zhang and S. Platnick, "An assessment of differences between cloud effective particle radius retrievals for marine water clouds from three MODIS spectral bands," *J. Geophys. Res.*, vol. 116, no. D20, p. 215, 2011, doi: 10.1029/2011JD016216.

[23] R. Pincus, S. Platnick, S. A. Ackerman, R. S. Hemler, and R. J. P. Hofmann, “Reconciling simulated and observed views of clouds: MODIS, ISCCP, and the limits of instrument simulators,” *J. Climate*, vol. 25, no. 13, pp. 4699–4720, Jul. 2012.

[24] S. Platnick, R. Pincus, B. Wind, M. D. King, M. A. Gray, and P. Hubanks, “An initial analysis of the pixel-level uncertainties in global MODIS cloud optical thickness and effective particle-size retrievals,” *Proc. SPIE*, vol. 5652, pp. 30–40, Dec. 2004.

[25] M. D. King, S. Platnick, W. P. Menzel, S. A. Ackerman, and P. A. Hubanks, “Spatial and temporal distribution of clouds observed by MODIS onboard the terra and aqua satellites,” *IEEE Trans. Geosci. Remote Sens.*, vol. 51, no. 7, pp. 3826–3852, Jul. 2013.

[26] M. D. King, S. Platnick, G. Wind, G. T. Arnold, and R. T. Dominguez, “Remote sensing of radiative and microphysical properties of clouds during TC^4: Results from MAS, MASTER, MODIS, and MISR,” *J. Geophys. Res.*, vol. 115, no. D10, pp. 1–15, May 2010, doi: 10.1029/2009JD013277.

[27] J. Riedi *et al.*, “Cloud thermodynamic phase inferred from merged POLDER and MODIS data,” *Atmos. Chem. Phys.*, vol. 10, no. 23, pp. 11851–11865, 2010.

[28] L. Liang, L. Di Girolamo, and S. Platnick, “View-angle consistency in reflectance, optical thickness and spherical albedo of marine water-clouds over the northeastern Pacific through MISR-MODIS fusion,” *Geophys. Res. Lett.*, vol. 36, no. 9, p. L09811, 2009, doi: 10.1029/2008GL037124.

[29] B. C. Maddux, S. A. Ackerman, and S. Platnick, “Viewing geometry dependencies in MODIS cloud products,” *J. Atmos. Ocean. Technol.*, vol. 27, no. 9, pp. 1519–1528, Sep. 2010.

[30] S. Zeng, C. Cornet, F. Parol, J. Riedi, and F. Thieuleux, “A better understanding of cloud optical thickness derived from the passive sensors MODIS/AQUA and POLDER/PARASOL in the A-Train constellation,” *Atmos. Chem. Phys.*, vol. 12, pp. 11245–11259, 2012, doi: 10.5194/acp-12-11245-2012.

[31] Z. Zhang, S. Platnick, P. Yang, A. K. Heidinger, and J. M. Comstock, “Effects of ice particle size vertical inhomogeneity on the passive remote sensing of ice clouds,” *J. Geophys. Res.*, vol. 115, no. D17, p. D17203, 2010, doi: 10.1029/2010JD013835.

[32] Z. Zhang, A. S. Ackerman, G. Feingold, S. Platnick, R. Pincus, and X. Huiwen, “Effects of cloud horizontal inhomogeneity and drizzle on remote sensing of cloud droplet effective radius: Case studies based on large-eddy simulations,” *J. Geophys. Res.*, vol. 117, no. D19, p. D19208, 2012, doi: 10.1029/2012JD017655.

[33] T. S. L’Ecuyer and J. H. Jiang, “Touring the atmosphere aboard the A-Train,” *Phys. Today*, vol. 63, no. 7, p. 36, 2010, doi: 10.1063/1.3463626.

[34] R. E. Holz *et al.*, “Resolving ice cloud optical thickness biases between CALIOP and MODIS using infrared retrievals,” *Atmos. Chem. Phys.*, vol. 15, no. 20, pp. 29455–29495, 2015, doi: 10.5194/acpd-15-29455-2015.

[35] C. J. Stubenrauch *et al.*, “Assessment of global cloud datasets from satellites: Project and database initiated by the GEWEX radiation panel,” *Bull. Amer. Meteorol. Soc.*, vol. 94, no. 7, pp. 1031–1049, Jul. 2013.

[36] S. Platnick *et al.*, “Assessment of IDPS VIIRS cloud products and recommendations for EOS-era cloud climate data record continuity,” NASA Goddard Space Flight Center, Greenbelt, MD, USA, Tech. Rep., Mar. 2013, p. 57. [Online]. Available: https://jointmission.gsfc.nasa.gov/DEW_NPP_reports/VIIRS%20Cloud%20Products%20Report%20(Mar-19-2013).pdf

[37] P. Minnis *et al.*, “CERES Edition-2 cloud property retrievals using TRMM VIRS and Terra and Aqua MODIS data—Part I: Algorithms,” *IEEE Trans. Geosci. Remote Sens.*, vol. 49, no. 11, pp. 4374–4400, Nov. 2011, doi: 10.1109/TGRS.2011.2144602.

[38] P. Minnis *et al.*, “CERES Edition-2 cloud property retrievals using TRMM VIRS and Terra and Aqua MODIS data—Part II: Examples of average results and comparisons with other data,” *IEEE Trans. Geosci. Remote Sens.*, vol. 49, no. 11, pp. 4401–4430, Nov. 2011, doi: 10.1109/TGRS.2011.2144602.

[39] P. Yang *et al.*, “Spectrally consistent scattering, absorption, and polarization properties of atmospheric ice crystals at wavelengths from 0.2 to 100 μm,” *J. Atmos. Sci.*, vol. 70, no. 1, pp. 330–347, Jan. 2013.

[40] M. J. Pavolonis and A. K. Heidinger, “Daytime cloud overlap detection from AVHRR and VIIRS,” *J. Appl. Meteorol.*, vol. 43, no. 5, pp. 762–778, May 2004.

[41] J. Sun *et al.*, “MODIS reflective solar bands calibration improvements in collection 6,” *Proc. SPIE*, vol. 8528, p. 85280N, Nov. 2012, doi: 10.1117/12.979733.

[42] C. B. Schaaf, J. Liu, F. Gao, and A. H. Strahler, “Aqua and Terra MODIS albedo and reflectance anisotropy products,” in *Land Remote Sensing and Global Environmental Change: NASA’s Earth Observing System and the Science of ASTER and MODIS*, B. Ramachandran, C. O. Justice, and M. J. Abrams, Eds. Springer, 2011, pp. 549–561.

[43] S. W. Seemann, E. E. Borbas, R. O. Knuteson, G. R. Stephenson, and H.-L. Huang, “Development of a global infrared land surface emissivity database for application to clear sky sounding retrievals from multispectral satellite radiance measurements,” *J. Appl. Meteorol. Climatol.*, vol. 47, no. 1, pp. 108–123, Jan. 2008.

[44] C. Cox and W. Munk, “Measurement of the roughness of the sea surface from photographs of the sun’s glitter,” *J. Opt. Soc. Amer.*, vol. 44, no. 11, pp. 838–850, Nov. 1954.

[45] R. C. Levy *et al.*, “The Collection 6 MODIS aerosol products over land and ocean,” *Atmos. Meas. Techn.*, vol. 6, no. 11, pp. 2989–3034, 2013.

[46] N. C. Hsu *et al.*, “Enhanced Deep Blue aerosol retrieval algorithm: The second generation,” *J. Geophys. Res.*, vol. 118, no. 16, pp. 9296–9315, Aug. 2013.

[47] S. Twomey and T. Cocks, “Remote sensing of cloud parameters from spectral reflectance in the near-infrared,” *Beitr. Phys. Atmos.*, vol. 62, no. 3, pp. 172–179, 1989.

[48] S. Twomey and T. Cocks, “Spectral reflectance of clouds in the near-infrared: Comparison of measurements and calculations,” *J. Meteorol. Soc. Jpn.*, vol. 60, no. 1, pp. 583–592, Jan. 1982.

[49] R. J. Curran and M.-L. C. Wu, “Skylab near-infrared observations of clouds indicating supercooled liquid water droplets,” *J. Atmos. Sci.*, vol. 39, no. 3, pp. 635–647, Mar. 1982.

[50] F. Rawlins and J. S. Foot, “Remotely sensed measurements of stratocumulus properties during FIRE using the C130 aircraft multi-channel radiometer,” *J. Atmos. Sci.*, vol. 47, no. 21, pp. 2488–2504, Nov. 1990.

[51] T. Nakajima, M. D. King, J. D. Spinhirne, and L. F. Radke, “Determination of the optical thickness and effective particle radius of clouds from reflected solar radiation measurements. Part II: Marine stratocumulus observations,” *J. Atmos. Sci.*, vol. 48, no. 5, pp. 728–751, Mar. 1991.

[52] Q. Han, W. B. Rossow, and A. A. Lacis, “Near-global survey of effective droplet radii in liquid water clouds using ISCCP data,” *J. Climate*, vol. 7, no. 4, pp. 465–497, Apr. 1994.

[53] P. Minnis, P. W. Heck, S. Mayor, and D. F. Young, “A near-global analysis of cloud microphysical properties,” in *Current Problems in Atmospheric Radiation*, W. L. Smith and K. Stamnes, Eds. Hampton, VA, USA: Deepak Publ., 1997, pp. 445–448.

[54] K. Stamnes, S.-C. Tsay, W. Wiscombe, and K. Jayaweera, “Numerically stable algorithm for discrete-ordinate-method radiative transfer in multiple scattering and emitting layered media,” *Appl. Opt.*, vol. 27, no. 12, pp. 2502–2509, Jun. 1988.

[55] G. M. Hale and M. R. Querry, “Optical constants of water in the 200-nm to 200-μm wavelength region,” *Appl. Opt.*, vol. 12, no. 3, pp. 555–563, Mar. 1973.

[56] K. F. Palmer and D. Williams, “Optical properties of water in the near infrared,” *J. Opt. Soc. Amer.*, vol. 64, no. 8, pp. 1107–1110, Aug. 1974.

[57] H. D. Downing and D. Williams, “Optical constants of water in the infrared,” *J. Geophys. Res.*, vol. 80, no. 12, pp. 1656–1661, Apr. 1975.

[58] B. H. Cole *et al.*, “Comparison of PARASOL observations with polarized reflectances simulated using different ice habit mixtures,” *J. Appl. Meteorol. Climatol.*, vol. 52, no. 1, pp. 186–196, Jan. 2013.

[59] H. C. van de Hulst, “The spherical albedo of a planet covered with a homogeneous cloud layer,” *Astron. Astrophys.*, vol. 35, no. 2, pp. 209–214, 1974.

[60] B. H. Kahn *et al.*, “Pixel-scale assessment and uncertainty analysis of AIRS and MODIS ice cloud optical thickness and effective radius,” *J. Geophys. Res.*, vol. 120, no. 22, pp. 11669–11689, 2015. [Online]. Available: http://dx.doi.org/10.1002/2015JD023950

[61] B. Marchant, S. Platnick, K. Meyer, G. T. Arnold, and J. Riedi, “MODIS Collection 6 shortwave-derived cloud phase classification algorithm and comparisons with CALIOP,” *Atmos. Meas. Techn. Discuss.*, vol. 8, no. 11, pp. 11893–11924, 2015.

[62] B.-C. Gao, A. F. H. Goetz, and W. J. Wiscombe, “Cirrus cloud detection from airborne imaging spectrometer data using the 1.38 μm water vapor band,” *Geophys. Res. Lett.*, vol. 20, no. 4, pp. 301–304, Feb. 1993.

[63] H.-M. Cho *et al.*, “Frequency and causes of failed MODIS cloud property retrievals for liquid phase clouds over global oceans,” *J. Geophys. Res.*, vol. 120, no. 9, pp. 4132–4154, May 2015.

[64] M. D. Lebsock, T. S. L'Ecuyer, and G. L. Stephens, "Detecting the ratio of rain and cloud water in low-latitude shallow marine clouds," *J. Appl. Meteorol. Climatol.*, vol. 50, no. 2, pp. 419–432, Feb. 2011.

[65] T. Y. Nakajima, K. Suzuki, and G. L. Stephens, "Droplet growth in warm water clouds observed by the A-Train. Part I: A multisensor view," *J. Atmos. Sci.*, vol. 67, no. 6, pp. 1897–1907, Jun. 2010.

[66] C. D. Rodgers, *Inverse Methods for Atmospheric Sounding: Theory and Practice*. Hackensack, NJ, USA: World Scientific, 2000, p. 238.

[67] V. Ramanathan and M. V. Ramana, "Persistent, widespread, and strongly absorbing haze over the himalayan foothills and the indo-gangetic plains," *Pure Appl. Geophys.*, vol. 162, no. 8, pp. 1609–1626, Aug. 2005.

[68] R. Gautam *et al.*, "Accumulation of aerosols over the indo-gangetic plains and southern slopes of the Himalayas: Distribution, properties and radiative effects during the 2009 pre-monsoon season," *Atmos. Chem. Phys.*, vol. 11, no. 24, pp. 12841–12863, Dec. 2011.

[69] U. C. Dumka *et al.*, "Latitudinal variation of aerosol properties from indo-gangetic plain to central Himalayan foothills during TIGERZ campaign," *J. Geophys. Res.*, vol. 119, no. 8, pp. 4750–4769, Apr. 2014.

[70] S. Platnick, "Vertical photon transport in cloud remote sensing problems," *J. Geophys. Res.*, vol. 105, no. D18, pp. 22919–22935, Sep. 2000.

[71] S. Platnick *et al.* (Oct. 2015). *MODIS Cloud Optical Properties: User Guide for the Collection 6 Level-2 MOD06/MYD06 Product and Associated Level-3 Datasets*. [Online]. Available: http://modis-atmos.gsfc.nasa.gov/_docs/C6MOD06OPUserGuide.pdf

Steven Platnick received the B.S. degree in electrical engineering from Duke University, Durham, NC, USA, in 1979, the M.S. degree in electrical engineering from the University of California at Berkeley, Berkeley, CA, USA, in 1980, and the Ph.D. degree in atmospheric sciences from the University of Arizona, Tucson, AZ, USA, in 1991.

He held engineering positions at Hewlett-Packard Company for six years and was a National Research Council Resident Research Associate with NASA Ames Research Center, Moffett Field, CA, Santa Rosa, CA, USA. He has been in collaboration with NASA Goddard Space Flight Center, Greenbelt, MD, USA, since 1993. He was a Research Associate Professor with the Joint Center for Earth Systems Technology, University of Maryland–Baltimore County, Baltimore, MD, USA, from 1996 to 2002. He joined NASA Goddard Space Flight Center in 2002, where he is currently the Deputy Director for Atmospheres in the Earth Science Division and a Senior Project Scientist with the Earth Observing System. He is a member of the MODIS Science Team and an Atmosphere Discipline Team Leader. His current research interests include theoretical and experimental remote sensing studies of clouds and aerosols.

Dr. Platnick is a Fellow of the American Meteorological Society.

Kerry G. Meyer received the B.S. degree in meteorology, and the M.S. and Ph.D. degrees in atmospheric sciences from Texas A&M University, College Station, TX, USA, in 2001, 2004 and 2007, respectively.

Since 2007, he has been in collaboration with NASA Goddard Space Flight Center, Greenbelt, MD, USA. From 2007 to 2010, he was a Post-Doctoral Fellow in the NASA Post-Doctoral Program managed by Oak Ridge Associated Universities, Oak Ridge, TN, USA. He was an Assistant Research Scientist with Goddard Earth Sciences and Technology, University of Maryland–Baltimore County, Baltimore, MD, USA, from 2010 to 2011. Since 2011, he has been a Research Scientist with Goddard Earth Science Technology and Research, Universities Space Research Association, Columbia, MD, USA. He is a member of the MODIS Science Team. His current research interests include satellite and aircraft remote sensing of clouds and aerosols.

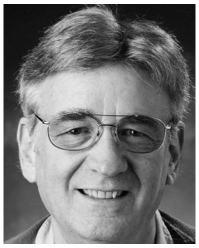

Michael D. King (M'01–SM'03–F'14) received the B.A. degree in physics from Colorado College, Colorado Springs, CO, USA, in 1971, and the M.S. and Ph.D. degrees in atmospheric sciences from the University of Arizona, Tucson, AZ, USA, in 1973 and 1977, respectively.

From 1978 to 2008, he was a Research Scientist with NASA Goddard Space Flight Center, Greenbelt, MD, USA, where he was a Senior Project Scientist with NASA's Earth Observing System from 1992 to 2008. Since 2008, he has been a Senior Research Scientist with the Laboratory for Atmospheric and Space Physics, University of Colorado at Boulder, Boulder, CO, USA. He is a Faculty Fellow with the Texas A&M University Institute for Advanced Study, Texas A&M University, College Station, TX, USA. He is a Team Leader of the MODIS Science Team. As a Team Member, he was responsible for the development of the cloud optical and microphysical property and Level-3 algorithms. His research experience includes conceiving, developing, and operating multispectral scanning radiometers from a number of aircraft platforms in field experiments ranging from arctic stratus clouds to smoke from the Kuwait oil fires in the Persian Gulf and biomass burning in Brazil and Southern Africa.

Dr. King is a Fellow of the American Geophysical Union, American Meteorological Society, and American Association for the Advancement of Science, and a member of the U.S. National Academy of Engineering. He was a recipient of the IEEE Prize Paper Award in 1993.

Galina Wind received the B.S. and M.S. degrees in computer science from the University of Illinois at Urbana–Champaign, Champaign, IL, USA, in 2000 and 2002, respectively, and the M.S. and Ph.D. degrees in atmospheric and oceanic science from the University of Maryland at College Park, College Park, MD, USA, in 2010 and 2016, respectively.

She has over 25 years of experience in advanced software development, signal processing, and data analysis at all levels from embedded real-time systems to high-performance computing applications. She was a member of the High Energy Physics Group, University of Illinois at Urbana–Champaign, from 1996 to 1998, and a member of the Laboratory for Computational Astrophysics at the National Center for Supercomputing Applications, University of Illinois at Urbana–Champaign, from 1998 to 2002.

She is a Senior Research Scientist with the Science Systems and Applications, Inc., Lanham, MD, USA, and has been a member of the MODIS cloud retrieval group since 2002. Her current research interests include modeling applications to radiative transfer to remote sensing involving a wide variety of satellite and aircraft instruments.

Nandana Amarasinghe received the B.Sc. (Hons.) degree in physics from the University of Peradeniya, Peradeniya, Sri Lanka, the M.S. degree in applied mathematics, and the Ph.D. degree in physics from Kent State University, Kent, OH, USA.

He is currently a Senior Scientific Programmer Analyst with Science Systems and Applications Inc., Lanham, MD, USA, and with NASA Goddard Space Flight Center (GSFC), Greenbelt, MD, USA. Since 2008, he has been a member of the Cloud Retrieval Group at NASA GSFC, where he is involved in radiative transfer modeling, algorithm development, and data analysis. He has also held positions at Remote Sensing Systems, Santa Rosa, CA, USA, and the University of Peradeniya, Peradeniya, Sri Lanka.

Benjamin Marchant received the Ph.D. degree in atmospheric science from the University of Science and Technology of Lille, Lille, France, in 2009.

He was a Post-Doctoral Fellow at the University of Maryland–Baltimore County, Baltimore, MD, USA, from 2010 to 2011, and NASA Goddard Space Flight Center (GSFC) through NASA Goddard Earth Sciences and Technology cooperative agreement. Since 2011, he has been a Research Scientist with the University Space Research Association and NASA GSFC through the NASA GESTAR (Goddard Earth Sciences Technology and Research) cooperative agreement. His current research interests include satellite remote sensing, machine learning, and image processing.

G. Thomas Arnold received the B.S. degree in metoerology and the M.S. degree in atmospheric science from the University of Wyoming, Laramie, WY, USA, in 1981 and 1986, respectively.

He is currently a Research Scientist with Science Systems and Applications Corp and has been collaborated with the Climate and Radiation Laboratory, NASA Goddard Space Flight Center, Greenbelt, MD, USA, since 1984. His research experience includes aircraft and satellite-based remote sensing of clouds and aerosols, specializing in data analysis via data visualization, data management, scientific software design, and radiometric instrument calibration.

Zhibo Zhang received the B.S. degree in atmospheric sciences from Nanjing University, Nanjing, China, in 2001, and the M.S. and Ph.D. degrees in atmospheric sciences from Texas A&M University, College Station, TX, USA, in 2004 and 2008, respectively.

Since 2008, he has been in collaboration with NASA Goddard Space Flight Center, Greenbelt, MD, USA. From 2008 to 2011, he was a Post-Doctoral Researcher in Science with Goddard Earth Sciences and Technology, University of Maryland–Baltimore County (UMBC), Baltimore, MD, USA. In 2011, he joined the Physics Department, UMBC, as a Faculty Member, where he is currently an Associate Professor. He is a member of the MODIS Science Team. His research interests include light scattering, radiative transfer, remote sensing of clouds and aerosols, and climate model evaluation and development.

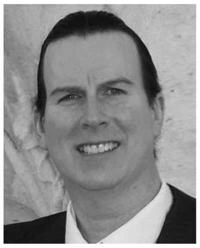

Paul A. Hubanks received the B.S. degree in mathematics from the University of Georgia, Athens, GA, USA, in 1979, and the M.S. degree in meteorology from Pennsylvania State University, University Park, PA, USA, in 1981.

He has more than 30 years of experience in satellite and aircraft data analysis and evaluation, solar and terrestrial research, scientific algorithm development and verification, software design-development-maintenance, data visualization, data analysis, and data management. In addition, he is an expert in designing and engineering state-of-the-art web sites and optimizing graphics and image data for the web, including the MODIS atmosphere web site. He is currently with Wyle Information Systems LLC, Lanham, MD, USA.

Robert E. Holz is an Associate Research Scientist with the Space Science and Engineering Center, University of Madison–Wisconsin, Madison, WI, USA, where he is currently an Associate Research Scientist with the Space Science and Engineering Center.

His current research interests include instrument intercalibration, the development of combined passive and active retrievals of clouds and aerosols, and the development of validation techniques using collocated aircraft and satellite observations.

Ping Yang received the B.S. degree in theoretical physics from Lanzhou University, Lanzhou, China, in 1985, the M.S. degree in atmospheric physics from the Lanzhou Institute of Plateau Atmospheric Physics, Chinese Academy of Sciences, Lanzhou, in 1988, and the Ph.D. degree in meteorology from the University of Utah, Salt Lake City, UT, USA, in 1995.

He is currently a Professor and the Head of the Department of Atmospheric Sciences with Texas A&M University, College Station, TX, USA, where he is the David Bullock Harris Chair in Geosciences. He has been actively conducting research in modeling of the optical and radiative properties of clouds and aerosols, in particular, ice clouds, and their applications to space-borne and ground-based remote sensing. He has co-authored 274 peer-reviewed journal publications and three books. His current research interests include remote sensing and radiative transfer.

Dr. Yang is a Fellow of the American Meteorological Society and the Optical Society of America. He was a recipient of the 2013 Ascent Award from the Atmospheric Sciences Section of the American Geophysical Union, where he is an elected Fellow. He serves as an Editor of the *Journal of the Atmospheric Sciences*.

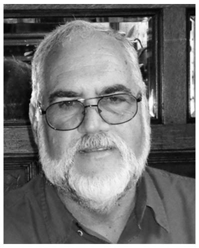

William L. Ridgway received the B.S. degree in physics and mathematics from the Massachusetts Institute of Technology, Cambridge, MA, USA, in 1974, and the Ph.D. degree in physics from the University of Chicago, Chicago, IL, USA, in 1981.

He supported the development of atmospheric radiative transfer models for the U.S. Air Force Geophysics Laboratory, Hanscom AFB, MA, USA, from 1979 to 1982. He was a Research Associate with the Department of Geosciences, Purdue University, Lafayette, IN, USA, from 1982 to 1984. He has been a Scientist with Applied Research Corporation and Science Systems and Applications, Inc. in collaboration with the Climate and Radiation Laboratory, NASA Goddard Space Flight Center, Greenbelt, MD, USA, since 1984. His research experience includes atmospheric radiation modeling, climate modeling, and satellite remote sensing of clouds and aerosols.

Jérôme Riedi received the B.S. degree in physics, and the M.S. and Ph.D. degrees in atmospheric sciences from the University of Lille, Villeneuve d'Ascq, France, in 1997, 1998, and 2001, respectively.

His Ph.D. research included the use of multiangle and polarization measurements from the Polarization and Directionality of the Earth's Reflectances/Advanced Earth Observation Satellite for determination of cloud microphysical properties. In 2001, he joined NASA Goddard Space Flight Center, Greenbelt, MD, USA, where he was a Research Associate for one year at the Goddard Earth Sciences and Technology Center, involved in MODIS cloud retrievals development and associated product quality assessment. He is currently a Professor with the University of Lille, and also a Research Scientist with the Laboratoire d'Optique Atmosphérique, where he is conducting research on clouds and aerosols properties retrieval with a special emphasis on the use of polarization and the development of a multisensor approach for clouds analysis.

Dr. Riedi is currently a member of the POLDER and GCOM-C/SGLI science teams and a member of the joint ESA/EUMETSAT Science Advisory Group for the Multiviewing-channel-polarisation Imager (3MI) mission in preparation for the European Polar System-Second Generation.